University of Alberta

Observations of BL Lacertae using the Solar Tower Atmospheric Cherenkov Effect Experiment

by

Daniel T. Wakeford

A thesis submitted to the Faculty of Graduate Studies and Research in partial fulfillment of the requirements for the degree of **Master of Science**.

Department of Physics

Edmonton, Alberta
Spring 2005

0-494-08167-8

Library and Archives Canada

Published Heritage Branch

395 Wellington Street
Ottawa ON K1A 0N4
Canada

Bibliothèque et Archives Canada

Direction du Patrimoine de l'édition

395, rue Wellington
Ottawa ON K1A 0N4
Canada

Your file *Votre référence*
ISBN:
Our file *Notre reference*
ISBN:

NOTICE:
The author has granted a non-exclusive license allowing Library and Archives Canada to reproduce, publish, archive, preserve, conserve, communicate to the public by telecommunication or on the Internet, loan, distribute and sell theses worldwide, for commercial or non-commercial purposes, in microform, paper, electronic and/or any other formats.

The author retains copyright ownership and moral rights in this thesis. Neither the thesis nor substantial extracts from it may be printed or otherwise reproduced without the author's permission.

AVIS:
L'auteur a accordé une licence non exclusive permettant à la Bibliothèque et Archives Canada de reproduire, publier, archiver, sauvegarder, conserver, transmettre au public par télécommunication ou par l'Internet, prêter, distribuer et vendre des thèses partout dans le monde, à des fins commerciales ou autres, sur support microforme, papier, électronique et/ou autres formats.

L'auteur conserve la propriété du droit d'auteur et des droits moraux qui protège cette thèse. Ni la thèse ni des extraits substantiels de celle-ci ne doivent être imprimés ou autrement reproduits sans son autorisation.

In compliance with the Canadian Privacy Act some supporting forms may have been removed from this thesis.

While these forms may be included in the document page count, their removal does not represent any loss of content from the thesis.

Conformément à la loi canadienne sur la protection de la vie privée, quelques formulaires secondaires ont été enlevés de cette thèse.

Bien que ces formulaires aient inclus dans la pagination, il n'y aura aucun contenu manquant.

Canada

Abstract

The Solar Tower Atmospheric Cherenkov Effect Experiment (STACEE) is a shower-front sampling atmospheric Cherenkov telescope which uses an array of solar heliostat mirrors as its primary optic. STACEE is designed to detect atmospheric Cherenkov radiation from extensive air showers due to astrophysical gamma rays with energies above 50 GeV.

Observations of the active galaxy BL Lacertae were made in the fall of 2002 using STACEE. A total of 2.5 hours of data were taken on the source, plus equivalent-duration background observations. After cuts, a total of 1.6 hours of live time remained, and a net on-source excess of 1001 events was seen above a background of 40987 events. At a significance of 4.7 σ this excess was insufficient to claim a detection of BL Lacertae. Assuming the EGRET spectral index of 2.4, the 95% confidence level upper limit on the gamma-ray flux was determined to be 2.4×10^{-9} cm^{-2} s^{-1} above 190 GeV.

Acknowledgements

I thank Dr. Doug Gingrich of the University of Alberta for his patient supervision of my research these past two years.

I thank the members of the STACEE collaboration. I especially thank Doug Bramel of Columbia University and Richard Scalzo of the University of Chicago for their detailed documentation of STACEE analysis methods. John Kildea of McGill University deserves my thanks for his much appreciated programming advice.

I thank the members of my thesis committee for their efforts during the examination period.

I thank my family for their love and support which to a great degree made this work possible.

Contents

1 Introduction 1

2 Gamma-Ray Astronomy 3

2.1 Satellites . . . 3

2.1.1 Early satellite experiments . . . 3

2.1.2 EGRET aboard the CGRO . . . 4

2.2 Ground-Based Experiments . . . 7

2.2.1 The Atmospheric Cherenkov Effect . . . 7

2.2.2 Imaging Cherenkov Detectors . . . 9

2.2.3 Shower-Front Sampling Cherenkov Detectors . . . 11

2.3 Future Detectors . . . 12

3 Active Galactic Nuclei 14

3.1 AGN Taxonomy . . . 14

3.2 Toward a generalized model . . . 15

3.2.1 Black Hole Central Engine . . . 16

3.2.2 Narrow and Broad Line Emitting Regions . . . 17

3.2.3 Relativistic Jets . . . 17

3.3 VHE Gamma-Ray Production . . . 18

3.3.1 Thermal Emission . . . 19

3.3.2 High Energy Particles and Fermi Acceleration . . . 20

3.3.3 Synchrotron Radiation . . . 21

3.3.4 The Inverse Compton Effect . . . 22

3.4 BL Lacertae . . . 23

3.4.1 Models for BL Lacertae . . . 25

3.5 Open Questions of AGN 27

4 The STACEE Detector **28**

4.1 Optics 28

4.1.1 Heliostats 29

4.1.2 Secondary Mirrors and PMT Cameras 30

4.2 Electronics 32

4.2.1 Flash Analog-to-Digital Converters 34

4.3 Simulations 35

4.3.1 CORSIKA 36

4.3.2 sandfield 36

4.3.3 elec 36

4.4 Applying Simulated Results to Real Data 37

4.4.1 Calculation of the Effective Area 37

4.4.2 Calculation of the Energy Threshold 38

5 Data Analysis **40**

5.1 stoff 41

5.2 Raw Data Calibration 41

5.3 Field-Brightness Asymmetry 42

5.3.1 Direct Measurement of the Promotion Effect 42

5.3.2 Library Padding in pass0 43

5.4 Data Quality 44

5.4.1 Data Cuts - Hardware Performance 44

5.4.2 Data Cuts - Level One Trigger Rate 45

5.5 Calculating the Significance 46

6 Noise Analysis **48**

6.1 Coherent Noise Estimation

Using Alternate Sums 50

6.2 Results - Time Dependence of Noise 51

6.3 Results - Component Dependence of Noise 53

6.4 Discussion 54

7 Observations of BL Lacertae **56**

7.1 Data Set 56

7.2 Cuts 57

7.3 Field Brightness Asymmetry 58

7.4 Simulation Inputs 60

7.4.1 CORSIKA Input 60

7.4.2 sandfield Input 61

7.4.3 elec Input 61

7.5 Flux 62

7.5.1 Energy Threshold Uncertainty 65

7.6 Discussion 65

8 Conclusion **68**

Bibliography **70**

List of Tables

3.1 Planck Law peak emission wavelengths. 19

6.1 FADC numbering. 53
6.2 Noise estimation by crate. Values are given in units of dc. . . 53
6.3 Noise estimation by board. Values are given in units of dc. . . 54
6.4 Averaged results, emphasizing components deviating from average component behaviour. 55

7.1 Raw data. 56
7.2 Final data. 58
7.3 Energy distribution of showers generated. 61
7.4 Summary of the important results of BL Lacertae observations. 66
7.5 BL Lacertae flux for several VHE gamma-ray experiments. . . 66

List of Figures

2.1 Total BATSE-detected GRBs in 1998. 5

2.2 The EGRET detector. 6

2.3 Location of sources of 0.1 – 10 GeV gamma-rays. 7

2.4 Various cosmic ray cascades. 8

2.5 At left, a charged particle moving at $v = 0.5\ c/n$, insufficient to generate Cherenkov light. At right, a Cherenkov shock front forms for a charged particle moving at $v = 1.33\ c/n$. The Cherenkov angle $\theta_C = arccos(cv^{-1}n^{-1})$. 9

2.6 Location of confirmed sources of 250 GeV gamma-rays. 11

3.1 AGN model. 16

3.2 Large-scale ordering of magnetic field, resulting in a collimated particle beam. 18

3.3 Second-order Fermi acceleration, showing both approaching and receding collisions. 21

3.4 First-order Fermi acceleration, showing repeated crossing of particle trajectory on central shock front. 21

3.5 Differential flux of BL Lacertae as a function of energy within the EGRET regime. 24

3.6 CIB attenuation of the observable percentage of flux from BL Lacertae. 24

3.7 Various hadronic model fits to the SED for BL Lacertae multi-wavelength observing campaign during 2000. EGRET data were not part of the campaign and are not considered by the fit. 25

3.8 Various leptonic model fits to the SED for BL Lacertae multi-wavelength observing campaign during 2000. EGRET data are not part of campaign and are not considered by fit. 26

4.1 The National Solar Thermal Test Facility. 29
4.2 The view from directly above the NSTTF. Heliostats used by STACEE are marked by the L1 trigger cluster to which they belong. 30
4.3 The central receiver tower, showing positions of secondary secondary mirrors as height above ground-level. 31
4.4 A side-on view of secondary mirror and camera. 32
4.5 A cross-section of PMT can assembly. 33
4.6 A side-on depiction of the angular acceptance of a DTIRC. . . 33
4.7 Basic STACEE electronics. 34
4.8 An example of hour angle measurement. 38

5.1 Example correlation plot for ON and OFF L1 trigger rates as recorded by one cluster. 45
5.2 Example histogram of θ showing a 2 σ cut on a Gaussian fit. . 46

6.1 FADC trace for a Cherenkov event. 49
6.2 Total, incoherent, and coherent components of noise over 24 hours. An average value for both total and incoherent noise is shown. 52
6.3 Magnified view of Figure 6.2, showing only the coherent noise. An average value for coherent noise is also shown. 52

7.1 Exposure-weighted histogram of pair significances. 58
7.2 BL Lacertae light-curve. 59
7.3 Promotion trend: excess trigger rate as a function of (ON-OFF) anode current difference. 60
7.4 L2 trigger rate as a function of hour angle. 62
7.5 HA-Averaged STACEE effective area plot for the positions of the BL Lacertae observations. 63

7.6 Differential trigger rate as a function of energy. 64
7.7 Gamma-Ray flux versus energy for BL Lacertae. Except for the EGRET detection, these are upper limits only. 67

Chapter 1

Introduction

During the 1990's, the Compton Gamma-Ray Observatory (CGRO) mapped the gamma-ray sky at photon energies below 10 GeV. This map revealed strong gamma-ray emission from the galactic plane, and a number of extragalactic point sources corresponding to active galaxies, pulsars, and supernova remnants. Results from the CGRO indicated that the flux of photons is related to their energy by an inverse power-law, and that the degree of the power-law is unique to each source. An extrapolation of this power-law indicated that many sources detected by the CGRO should also be detectable at TeV energies. Ground-based detectors, their sensitivities limited to the TeV regime and higher, are unable to detect many of these sources. Where did all the sources go? This question can only be answered by using a detector sensitive to intermediate gamma-ray energies 10−300 GeV − the "unopened window".

The Solar Tower Atmospheric Cherenkov Effect Experiment (STACEE) was conceived and constructed during the mid-1990's upon the existing infrastructure of the solar research facility at Sandia National Laboratories in New Mexico. STACEE is one of the first generation of shower-front sampling atmospheric Cherenkov detectors, and is able to detect gamma-rays of energy $\sim$ 100 GeV. During 2000, STACEE detected strong emission from the Crab Nebula above 190 GeV, at the time the lowest energy threshold achieved by a ground-based shower-front sampling detector. In 2002, STACEE detected strong, variable emission from the active galaxy Markarian 421, and in 2004 reported no gamma-ray emission from observations of the active galaxy

W Comae. These results, whether positive or null, place constraints on the theoretical models proposed for each active galaxy. These models attempt to explain the observed spectral energy distribution of photons from each source. A valid model must consider observations conducted at all wavelengths of the electromagnetic spectrum.

The position of active galaxy BL Lacertae has been observed by detectors operating at all available wavelengths, but gamma-rays above 10 GeV have not been detected. Various models of the composition and behaviour of BL Lacerate have been proposed. A detection of BL Lacertae at STACEE energies would be strong evidence for an energetic population of hadrons near the core, while a null result would not rule out either hadronic or leptonic emission models.

This thesis discusses the history and current state of gamma-ray astronomy (Chapter 2), the theory of active galaxies (Chapter 3), the STACEE experiment and data analysis techniques (Chapters 4 and 5), and the results and implications of STACEE's observations of BL Lacertae (Chapter 7). Included with this source analysis is an investigation of noise within the electronics at STACEE (Chapter 6). Specifically discussed is the degree of coherent noise in the electronics used for data acquisition. It is important to quantify any coherent noise since noise reduction will allow STACEE greater sensitivity at lower gamma-ray energies.

Chapter 2

Gamma-Ray Astronomy

The science of astronomy has evolved simultaneously with improvement in technology. As new equipment was availed them, astronomers were able to examine increasingly subtle layers of the sky. Radiation exists in space at all observable photon wavelengths, but for centuries only the optical band of the electromagnetic spectrum had been accessible to humans. Well before their detection, the existence of high energy astrophysical gamma-rays was predicted by theory. Gamma-Rays can be produced by several processes: interaction of cosmic rays with interstellar gas, violent supernova explosions, interaction of charged particles with strong magnetic fields of active galactic nuclei, and in mysterious gamma-ray bursts.

2.1 Satellites

Placing a detector above the Earth's atmosphere is the only way to directly detect astrophysical gamma-rays. Satellite detectors can run continuously and with a wide field of view. Unfortunately they are expensive to build and difficult if not impossible to maintain.

2.1.1 Early satellite experiments

The first unambiguous detection of gamma-rays was made in 1961 by the Explorer XI satellite. Over 23 days, it detected 22 gamma-ray photons amid 22000 cosmic rays. The detector was sensitive to gamma radiation above 50 MeV. In 1967, the satellite OSO-3 recorded 621 cosmic gamma-rays above

50 MeV with an anisotropic distribution concentrated about the galactic equator. Gamma-Ray sensitivity and detector resolution continued to improve and with higher statistics came more interesting results. The first dedicated gamma-ray satellite SAS-2 was launched in 1972 and observed gamma-rays of energies 20−1000 MeV, confirming the anisotropic background seen by earlier experiments as well as hinting at possible point sources away from the galactic equator. From 1975−1982 the satellite COS-B found similar results with a widened energy range 2 keV−5 GeV. These two experiments heralded great advances in technology, but their spatial and energy resolutions were inadequate to make confident conclusions about the precise location of point sources or the energy spectrum of these high energy particles. Gamma-Ray bursts, not anticipated by theory, were observed with great excitement from 1969−1972 aboard the Vela series of satellites. The Vela shield was launched to police the adherence of several signatory nations to a recently signed nuclear test ban treaty, promising the cessation of nuclear bomb detonation in the atmosphere. Vela carried x-ray, gamma-ray and neutron detectors. A strong x-ray flash accompanied by gamma-rays and possibly neutrons would be conclusive evidence of a nuclear bomb blast. Extracurricular to its intended purpose, Vela recorded 73 astrophysical gamma-ray bursts. This was the first observation of high-flux transient gamma-ray sources that quickly fade. Multiple bursts from the same location were not observed [1].

2.1.2 EGRET aboard the CGRO

The Compton Gamma-Ray Observatory (CGRO) [2] was launched in 1991 and collected data for a decade. The CGRO housed the four experiments listed below, each uniquely designed to probe the universe for gamma-rays.

BATSE - The Burst and Transient Source Experiment was a spectrometer operating between 20−600 keV, studying fast-changing sources like gamma-ray bursts (GRBs), with a wide field of view.

OSSE - The Oriented Scintillation Spectrometer Experiment was a pointable instrument with a narrow field of view designed to focus on transient

BATSE sources, operating between 0.05−10 MeV.

Comptel - The Imaging Compton Telescope produced images of the gamma-ray sky, for sources emitting photons between 0.8−30 MeV.

EGRET - The Energetic Gamma-Ray Experiment Telescope pointed at the same locations as Comptel, taking specific measurements of photon energy within the range 0.02−30 GeV.

BATSE dismissed the hypothesis that gamma-ray bursts originate only from the galactic plane. BATSE detected an average of six GRBs per week over its observing lifetime; the distribution is shown in galactic coordinates in Figure 2.1 [3] with the galactic centre at the centre of the plot. For observing

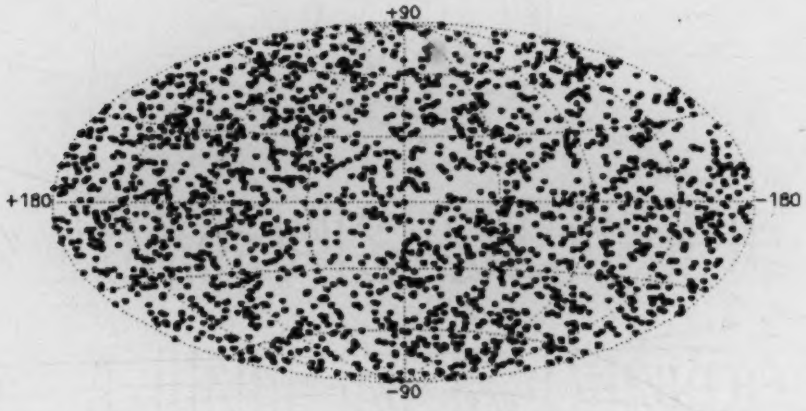

Figure 2.1: Total BATSE-detected GRBs in 1998.

the general gamma-ray sky, EGRET was limited by its small size (~ 0.15 m^2); reliable only up to 10 GeV. EGRET produced a stunning image of the gamma-ray sky, showing strong emission from sources in both the galactic plane and extragalactic space. Several critical components allow EGRET (Figure 2.2 [4]) to view gamma-rays. An anti-coincidence scintillator houses the entire experiment. It is made of material that emits a flash of light upon interaction with charged particles (e.g. cosmic rays) while allowing neutral particles (e.g. photons) to pass quietly. If there is signal from the shield, no data are

recorded for an interval of time. In this way, the isotropic cosmic ray background is eliminated, and only gamma-rays are recorded. A dense converter material mediates electromagnetic pair-production, and the resulting leptons excite scintillator crystals in the detector base. Signal from the crystals is collected to measure the energy of the incident gamma-ray.

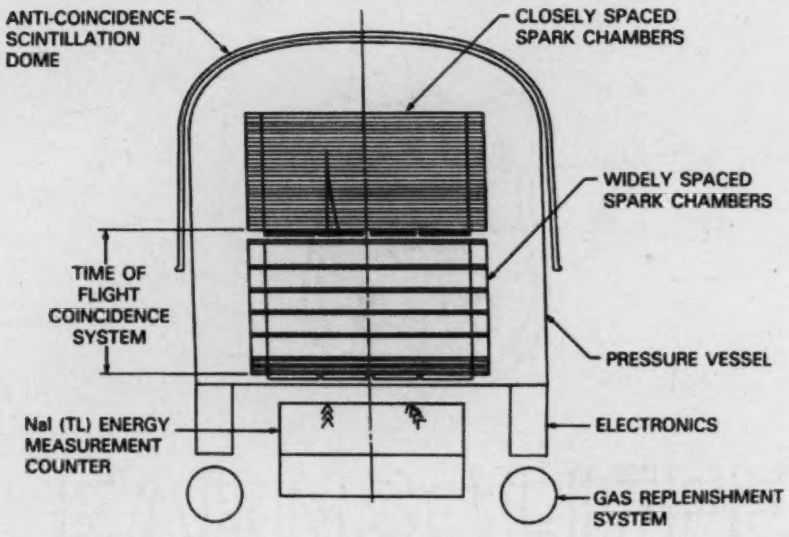

Figure 2.2: The EGRET detector.

EGRET detected 271 sources emitting gamma-rays with energies 0.1−10 GeV [5]. The source positions are plotted in galactic coordinates in Figure 2.3 [4].

EGRET results indicate that the flux F of photons of a given energy E is related to that energy by a power law $F \sim E^{-\alpha}$, for which $2 < \alpha < 3$. Extrapolating this result to higher energies indicates that the extragalactic point sources specified by EGRET are potentially observable from Earth. It is the job of ground-based experiments to examine the emission spectra of these sources at a higher energy range (>10 GeV).

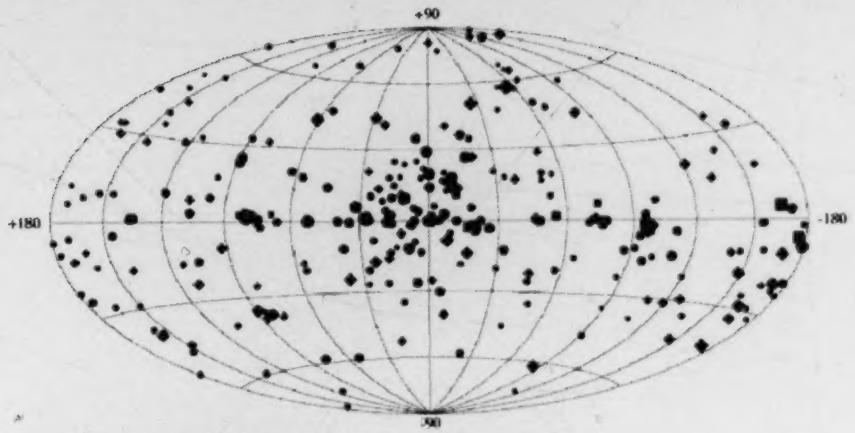

Figure 2.3: Location of sources of 0.1 – 10 GeV gamma-rays.

2.2 Ground-Based Experiments

Since the Earth's surface is shielded from gamma radiation by the atmosphere, it is not possible to collect gamma-ray photons on the ground. However, it is possible to detect evidence of the high energy interactions of gamma-ray photons with atmospheric nuclei, by collecting the resultant Cherenkov photons. Ground-based detectors are marred by a reliance on clear, static night sky weather for observations, and unavoidable large cosmic ray backgrounds.

2.2.1 The Atmospheric Cherenkov Effect

Photons that are not attenuated in extragalactic space travel great distances to impinge upon the Earth's atmosphere. The very small wavelength of these photons makes them highly susceptible to interaction with light nuclei in the atmosphere. By comparison, visible and optical photons have wavelengths which are too large to interact in this way. In the presence of an atmospheric nucleus, a gamma-ray photon will undergo a process called pair-production, which transforms a photon into an electron-positron pair. These two particles continue toward Earth, slowing down rapidly in the dense atmosphere. The

process of slowing down involves emitting radiation in the form of high energy photons, and is typically called bremsstrahlung, or "braking radiation". These bremsstrahlung photons subsequently undergo pair production. As this process continues, the number of particles in this electromagnetic cascade increases geometrically, until it suddenly stops. Intuitively, the shower should stop when bremsstrahlung photons are of energy E < 1.02 MeV = 2 $m_e c^2$, and pair production is no longer possible by conservation of energy. The actual threshold is much higher than this. Once the leptons are below about 83 MeV, ionization usurps bremsstrahlung as the dominant radiative process, and the shower ceases to grow. The result is a conical shape called an extensive air shower (Figure 2.4 [6]).

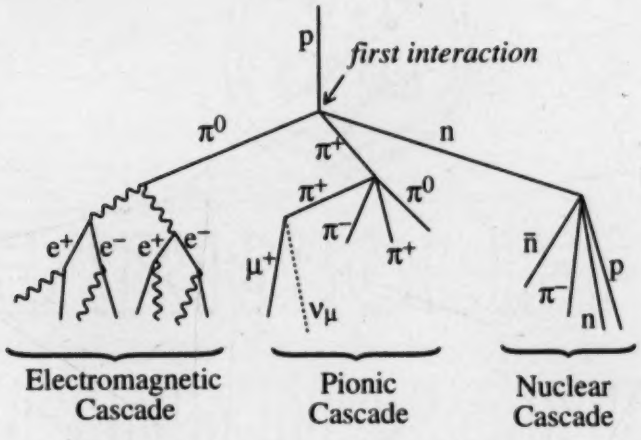

Figure 2.4: Various cosmic ray cascades.

An extensive air-shower can initiate a second-order process called the atmospheric Cherenkov effect. High energy charged particles traveling through a medium cause disturbances in that medium. As they slow down, high energy charged particles can travel for brief intervals at speeds greater than the local speed of light $v_{light} = c/n$, where n is the refractive index of the atmosphere, varying with elevation. This high speed condition produces an impulse on ambient nuclei in the atmosphere. From the point of view of one of these nuclei, a rapidly time-varying electric field has been abruptly switched on in its immediate vicinity, which is the condition required for the atom to radiate. The

net effect is for the radiation caused by these disturbances to add coherently to form a shock-front of light. This shock front is Cherenkov light.

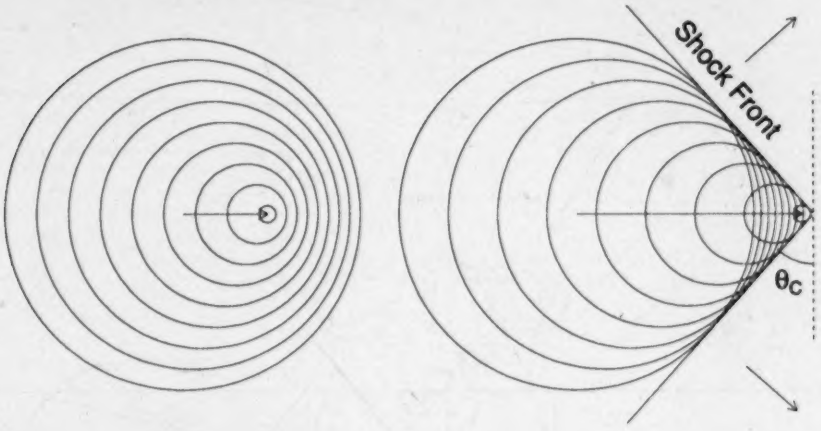

Figure 2.5: At left, a charged particle moving at $v = 0.5\ c/n$, insufficient to generate Cherenkov light. At right, a Cherenkov shock front forms for a charged particle moving at $v = 1.33\ c/n$. The Cherenkov angle $\theta_C = arccos(cv^{-1}n^{-1})$.

For atmospheric gamma-rays, the spectrum of Cherenkov light peaks at near-ultraviolet wavelengths. Knowing the lateral distribution on Earth of Cherenkov light can hint at the position of the incident gamma-ray, while the density of Cherenkov light can suggest an incident energy.

2.2.2 Imaging Cherenkov Detectors

Imaging Atmospheric Cherenkov Telescopes (IACTs) are the most established ground-based gamma-ray detectors. An IACT consists of a single dish comprised of many facets which reflects Cherenkov light to a focal point at which there is a pixellated camera of photomultiplier tubes. An image of the Cherenkov distribution is recorded. Typically, for gamma-ray induced showers, the Cherenkov distribution is even about some central core and elliptical in shape. Hadronic showers include several particle species of differing mass, leaving a more asymmetric scattering of Cherenkov photons. So, parameterizing all captured images in terms of size and shape, it is possible to define parameter bounds for which an image is considered with high certainty to

relate to a gamma-ray. Images lying outside those bounds are hadronic showers and are rejected from further analysis. The accepted gamma-ray images can then be used to reconstruct the arrival direction and the energy of the incident gamma-ray photon. The pioneering single-dish IACT is the Whipple Observatory in Arizona [7]. The prototype version of 10 m-diameter Whipple telescope made the first ground-based detection of high-energy gamma-rays from the Crab Nebula in 1989. One drawback to single-dish IACTs like Whipple is their sensitivity to muons. Muons can be created in a hadronic cascade and then can cause a muonic cascade similar to a gamma-ray induced electromagnetic cascade. In some situations, collected Cherenkov distributions from muonic cascades might not be excluded from analysis on the basis of parameterization cuts. An effective way to eliminate this is to have several single-dish IACTs working in unison. This stereoscopic imaging is employed by several collaborations, for example HEGRA [8]. The Japanese-Australian CANGAROO collaboration during the late 1990's used a 3.8 m-diameter single dish IACT to collect Cherenkov light from 2 TeV gamma-rays, and has since upgraded to a larger 10 m-diameter telescope with plans to incorporate stereoscopic imaging to lower the energy threshold to 100 GeV [9]. In addition to solving the muon problem, a stereoscopic array of IACTs increases the collecting area of the experiment, allowing access to a lower energy regime. As of January 2003, ground-based observation had revealed that very few EGRET sources emit gamma rays at energy greater than 250 GeV (Figure 2.6) [10].

Based on a high energy extrapolation of the power-law flux-energy relation, more of these sources should be detectable at 250 GeV. That they are not detectable leads to several possible conclusions. First, since a power-law dependence extends asymptotically to infinite energy, the total flux is arbitrarily (hence nonphysically) large, meaning there must be a spectral cut-off at some energy, perhaps below 250 GeV. Second, perhaps the observations were made during periods of low activity. Highly variable sources may require longer times of observation. Third, the gamma-ray photons may be absorbed before they reach Earth's atmosphere. This absorption takes the form of a photon-photon annihilation to an electron-positron pair. The second pho-

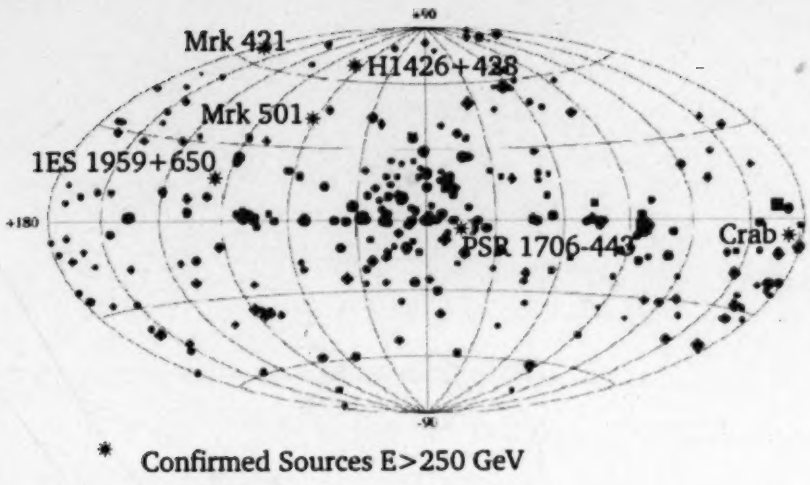

Figure 2.6: Location of confirmed sources of 250 GeV gamma-rays.

ton is attributed to extragalactic background light (EBL). EBL cutoff can be used to explain the lack of high energy gamma rays for distant sources since the probability of such an interaction increases with source distance. Sources at small redshifts are not thought to be susceptible to EBL absorption [11]. Whatever the case, something interesting must happen to photon flux within the energy range inaccessible to both EGRET and the present IACTs. This unopened window exists between approximately 50−300 GeV. The next generation of IACTs [12] and the next gamma-ray satellite [13] will close this gap. While these are being built, a new type of detector has been developed to observe the unopened window.

2.2.3 Shower-Front Sampling Cherenkov Detectors

Competing with the IACTs are detectors based on the shower-front sampling technique. In contrast to the precision and small size of IACTs, shower-front samplers can be inexpensively built using the framework of a solar energy collection facility [6]. The large collecting area of such a detector allows observation at a lower energy than accessible to IACTs. Shower-Front samplers record photon energies and arrival times but cannot record precise informa-

tion about photon arrival directions. This disallows the use of the IACT technique using angular photon distributions to remove cosmic-ray shower photons. Shower-Front samplers rely on the local isotropy of the cosmic ray background to distinguish gamma-ray signal from background fluctuations. STACEE is the pioneer shower-front sampler. Similar instruments are CELESTE [14] and Solar-2 [15]. Shower-Front sampling is a technique that was quickly developed and implemented to get results within the unopened window. STACEE has confirmed gamma-ray emission from the Crab Nebula (above 190 GeV) [6] and from the active galaxy Markarian 421 (above 140 GeV) [16]. In addition to observing source positions detected by EGRET, STACEE is used to record signal from the enigmatic GRBs. Owing to our lack of understanding, it is important to continue GRB observations in the interim while no gamma-ray satellite is in orbit.

2.3 Future Detectors

The Large Area Telescope (LAT) aboard GLAST will do a survey of 20 MeV to 300 GeV photons [17]. LAT is an updated EGRET, incorporating newer technologies for faster data acquisition, better background rejection, and more accurate pointing resolution. In addition to important hardware updates, the physical size of GLAST ($\sim$ 1 m^2) allows the possibility of access to higher energies than its predecessor. GLAST is scheduled to launch in February, 2007. Ground-based detectors are also improving. The VERITAS stereoscopic IACT array predicts a threshold of 75 GeV [12]. The MAGIC detector claims it will be sensitive to gamma-rays 10$-$300 GeV [18]. Much interest is generated by the HESS experiment; a second generation stereoscopic IACT array built in the desert of Namibia, which published its first results in 2004 [19]. The second generation of IACTs, combined with GLAST, will close the unopened window in an effort to obtain full multi-wavelength spectra of gamma-ray emitting sources. Multi-Wavelength data, ideally contemporaneous, will gives a comprehensive picture of the gamma-ray emission from galaxies with active nuclei (AGN), energetic pulsars, supernova remnants, and

other sources which appear to defy classification.

Chapter 3

Active Galactic Nuclei

Astrophysical gamma-ray photons have energies of MeV and higher. Initially, it was thought that these high energy particles could be produced by thermal means like their less energetic counterparts. In the laboratory, gamma-rays are produced through the excitation of matter on a nuclear scale, much like x-rays are produced by excitation at the atomic scale. As the science of galaxies with active nuclei (AGN) developed, it became apparent that the physical size of AGN combined with the required surface temperatures for thermal production led to a unlikely model. More exotic processes were considered, and were found to closely match some observations. As detector technology advanced with theory, a coherent though still contested model of AGN took shape. This model partly consolidates the wildly varied taxonomy that continues to plague this science.

3.1 AGN Taxonomy

Under the banner name of AGN reside several types of galaxies which exhibit characteristics varying to such a degree that they could not, with the models of the past, be thought of as familial. To understand the development of the unified model of AGN (Figure 3.1), it is useful to discuss past observational taxonomy [20]. Radio-Loud AGN are so named if the intensity of radio-wavelength photon emission exceeds that of optical-wavelength photon emission by a factor of 10. Of the Radio-Quiet AGN, Seyfert galaxies have visible spiral structure and core-dominated optical emission. Seyfert Type 1

galaxies show both narrow and broad line emission, while Seyfert Type 2 galaxies show only narrow lines. Quasars are Type 1 Seyfert galaxies, but the extended galactic structure is not visible, so that they appear as a point source of light (i.e. QUASi-stellAR). Of the Radio-Loud AGN, Fanaroff-Riley Type 2 galaxies have jet-dominated emission and are optically bright. These are separated by the spectral index α (Photon Flux $\propto$ Energy$^{-\alpha}$) of the characteristic radio emission. The spectrum is steep (SSRQ) if $\alpha > 0.5$ and flat (FSRQ) otherwise. By contrast, Fanaroff-Riley Type 1 galaxies have core-dominated emission and are optically faint. A subset of these are BL Lacertae-type objects, so named for their prototype, which show weak or absent optical emission lines. These emit radiation over the entire electromagnetic spectrum, with two distinct yet broad maxima in intensity. The high energy peak is in the gamma band, while the low energy peak is either in the radio or x-ray band. Conventionally, BL Lacertae objects are further divided based on the frequency regime of their low-energy peak, either radio (or low energy) BL Lacertae (RBL, LBL), or x-ray (or high energy) BL Lacertae (XBL, HBL). Recently, this final sub-categorization has been discredited as a serious distinction in the physical structure of a BL Lacertae object [21]. W Comae, for example, has a low-energy spectral peak between the XBL and RBL regimes, suggesting that these two are mere extrema of a more continuously distributed class of objects.

3.2 Toward a generalized model

The sub-categorization of AGN reflects our ability to observe only a small angular component of the flux from a source. It has been widely speculated that the varied taxonomy of AGN can be attributed principally to the orientation of the galactic major axis with respect to our line of sight. Present models restrict the flux of radiation, not allowing isotropic emission at all wavelengths. Perhaps mixing the conditions of orientation with those of age can collect AGN together as one family of objects, unifying the fragmented taxonomy above. This is the goal of generalized models of AGN, which typically include components such as a central, rotating super-massive black hole ac-

creting surrounding gas and dust, the gravitational potential energy of which being released along collimated jets forming a major axis. The structure is threaded by magnetic fields, and may resemble Figure 3.1. It is useful to explain in detail the evidence for this proposed model.

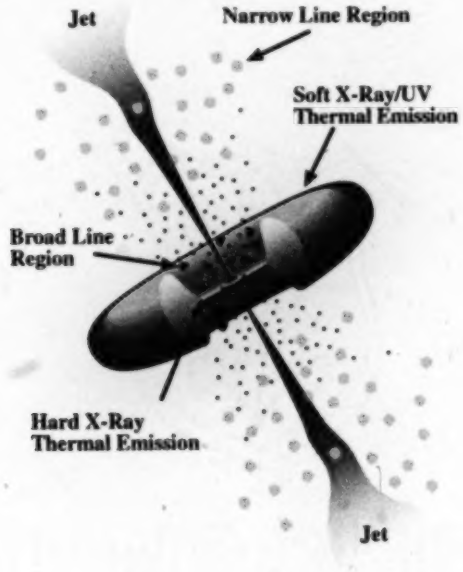

Figure 3.1: AGN model.

3.2.1 Black Hole Central Engine

Causality implies that the intensity of radiation from a source cannot vary on timescales less that the light-crossing time of the source. Expressly, $\Delta t \not< R/c$, where R is the size of the source object. Highly variable objects are, by this condition, constrained in size. This, coupled with the great amount of emission from AGN, implicates a super-massive black hole compact object as the central engine of any AGN. A problem with using the black hole is the tendency of all surrounding matter to quickly fall radially inward to a central singularity from which there is no escape. There is observational evidence for a dense torus of gas and dust accreting and rotating about the black hole. Some theories assume there is some initial net angular momentum to the accreting matter, but differ about how this momentum is obtained [22].

3.2.2 Narrow and Broad Line Emitting Regions

The tools of emission spectroscopy are used to ascertain the physical size of an AGN. The broad and narrow line regions of Figure 3.1 are composed of diffuse light-element gases. These gases are identified by monitoring the spectrum of emitted radiation. Every element has a unique spectral pattern showing high intensity of radiation at certain wavelengths. These peak regions are called spectral lines. By the theory of atomic transitions, spectral lines should exist at a precise wavelength with no deviation. In practice there are conditions which can cause either a shift of the position or a broadening of the width of a spectral line. Observations of a source moving at constant velocity will reveal spectral lines that are shifted in wavelength owing to the Doppler shift. Similarly, the width of characteristic spectral lines can be taken as a measure of a rotating object's physical size. The width (or distribution in wavelength) of a spectral line is a direct result of the Doppler shift of emitted radiation. As an object rotates, an observer will record a greater Doppler shift between approaching and receding matter. This smears a spectral line about some mean characteristic wavelength. The width of the smearing will give a measure of the speed of rotation of that object. An annulus of gas close to the core of the rotating AGN will rotate more quickly than annuli on the perimeter. These are the broad and narrow line emitting regions, respectively. In some cases the broad lines are not observed, suggesting side-on orientation of the AGN and opacity of the dense torus.

3.2.3 Relativistic Jets

The AGN core outshines any fine detail of galactic structure. The only distinguishable feature outside the core is the extended collimated jet structure which dramatically extends out to hundreds of kiloparsecs. The formation of jets is not well understood, and competing theories cannot yet explain both the size and collimation of the jets while remaining consistent with the more established theories of core nuclear structure. An intuitive possibility is that perhaps the radiation in the jets is an unattenuated subset of a spherical

outflow from the core, with much of this radiation lost in a torus which acts as a funnel, collimating the jet. This does not adequately explain the highly relativistic nature of the jets. A possible addition is a large magnetic field structure threading the accretion disk. The field lines become twisted as the disk rotates (Figure 3.2 [22]), effectively collimating the beam.

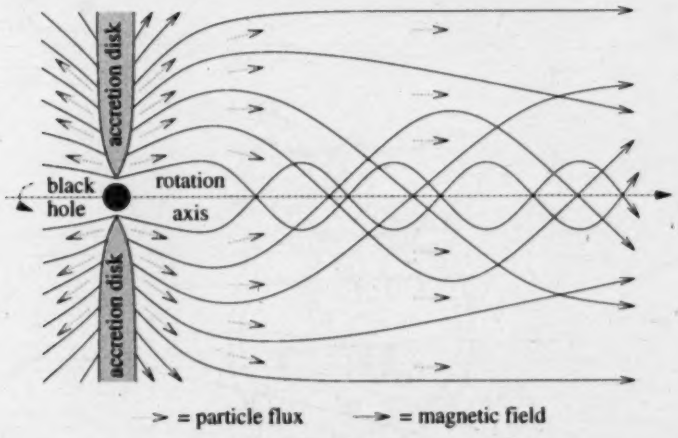

Figure 3.2: Large-scale ordering of magnetic field, resulting in a collimated particle beam.

3.3 VHE Gamma-Ray Production

The previous section describes a proposed physical structure for AGN. Upon that general framework can be constructed theories of very high energy (VHE) gamma-ray production in AGN. Below the x-ray regime, radiation is a by-product of nucleosynthesis. X-Rays can be produced thermally if sufficient temperatures are reached, but can also be produced through x-ray fluorescence. Gamma-ray emission from AGN is thought to be non-thermal, in that it is attributable entirely to relativistic processes. The spectral lines observed in AGN correspond to gas temperatures which reach over a million degrees Kelvin, and their spectral line-widths indicate bulk rotational velocities approaching one thousand kilometres per second. The volume and density of matter required to achieve this extreme temperature is many times larger than what is permitted by the causality restriction which relates radiative variability to object size.

AGN size rules out any thermal emission mechanism for gamma-rays, leaving other more exotic processes to be considered.

3.3.1 Thermal Emission

Electromagnetic radiation can be generated by the movement of particles. For example, a gas with fast moving constituent particles emits more heat than one which is less excited. The behaviour of this thermal (also called blackbody) emission mechanism is understood to obey the Planck Law relating intensity to wavelength (Equation 3.1). The Planck Law describes a continuous distribution in intensity

$$I_\lambda = \frac{2hc^2}{\lambda^5} \frac{1}{e^{\frac{hc}{\lambda kT}} - 1}, \tag{3.1}$$

with a peak wavelength determined by the temperature of the gas. The hotter gas emits more radiation distributed about a smaller peak wavelength. Using the Wien approximation to the Planck Law for small wavelengths $\left(e^{\frac{hc}{\lambda kT}} - 1 \rightarrow e^{\frac{hc}{\lambda kT}}\right)$, the peak of the spectrum is resolved to

$$\lambda_{peak} = \frac{0.029}{T}. \tag{3.2}$$

Some sample objects, their approximate temperatures, corresponding peak wavelengths, and the matching region of the electromagnetic spectrum are listed in Table 3.1. CMB and CIB refer to sections of the spectrum of cosmic background radiation (also called extragalactic background light) at microwave and infrared wavelengths, respectively.

Object	Temperature (K)	λ_{peak}	Region
CMB	2.7	2 mm	Microwave
CIB	27	0.1 mm	Infrared
Human	310	9.4 μm	Infrared
Sun	6000	480 nm	Visible
Hot Star	30000	970 nm	Ultraviolet
Intra-Cluster Gas	10^8	29 pm	X-Ray
AGN	$> 10^9$	< 1 pm	Gamma-Ray

Table 3.1: Planck Law peak emission wavelengths.

Adding the light at all wavelengths will yield the thermal luminosity of the object. Luminosity L is related to object radius R and temperature T by $L = 4\pi R^2 \sigma T^4$, where σ is the Stefan-Boltzmann constant. A small object observed at high luminosity must exist at high temperatures. AGN are observed at high luminosity and small size such that the temperature required, coupled with the small population of particles available to generate such heat, make thermal emission an unlikely mechanism for the production of gamma-rays.

3.3.2 High Energy Particles and Fermi Acceleration

To non-thermally produce high energy photons, a population of high energy electrons, protons, or some admixture of the two is required. It is common to explain the production of high-energy particles through Fermi acceleration, theorized by its namesake as an explanation of the observed spectrum of cosmic rays. Fermi acceleration is the repeated reflection of a charged particle from the plane of the interstellar magnetic field. This field contains mobile inhomogeneities of either direction or magnitude called kinks, which act as magnetic mirrors. The charged particle undergoes a series of collisions with these kinks, with equal probability of an approaching or receding collision. In an approaching collision, the particle gains energy, while in a receding collision, the kink gains energy. Over time there should be more approaching than receding collisions, causing the particle to gain energy. This is more accurately described as second-order Fermi acceleration (Figure 3.3 [22]), since the particle's energy gain in an observers rest frame depends on the square of the kink velocity.

In violent explosions, if one fluid expands into another at greater than the speed of sound in the slow medium, a shock front is formed. The shock front passes through the medium at a speed not greater than the speed of sound, so that in the rest frame of the shock front, both the slow and fast moving fluids flow toward it. A free charged particle in the fluid will be repeatedly drawn through the shock front, scattering in each instance from magnetic kinks either ahead of or behind the front, gaining energy in each instance until it escapes the system or loses energy through some other mechanism (e.g. inelastic collision).

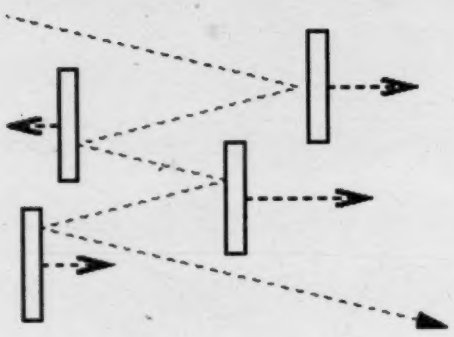

Figure 3.3: Second-order Fermi acceleration, showing both approaching and receding collisions.

Since the energy gain of the particle is dependent linearly on the shock front velocity, this is called first-order Fermi acceleration (Figure 3.4 [22]).

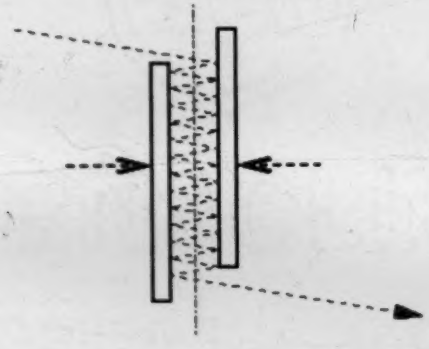

Figure 3.4: First-order Fermi acceleration, showing repeated crossing of particle trajectory on central shock front.

3.3.3 Synchrotron Radiation

A particle moving at velocity $\beta = v/c$ with Lorentz factor $\gamma = (1-\beta^2)^{-1/2}$, in a magnetic field of strength B will travel in a helical pattern with synchrotron frequency

$$\nu = \frac{eB}{2\pi\gamma mc}. \tag{3.3}$$

This constant centripetal acceleration causes the particle to emit synchrotron radiation. The functional form for total power emitted, P, relates

magnetic field strength, particle energy, and helical pitch angle α by

$$P = \frac{\sigma_T}{4\pi}\left(\frac{m_e}{m}\right)^2 c(\beta\gamma B \sin\alpha)^2, \tag{3.4}$$

where σ_T is the cross-section for Thomson scattering. The process of synchrotron radiation accounts for the low energy emission of AGN, either in the X-ray regime (XBLs) or the radio (RBLs). Since synchrotron radiation intensity is inversely proportional to the mass of the radiating particle, electrons are a more attractive candidate than protons. The high energy emission involves particle energies too great to be attributed to synchrotron radiation.

3.3.4 The Inverse Compton Effect

A low energy photon can be significantly boosted in energy by a collision with a high energy particle, a process described by a frame-shifted (or inverse) Compton effect. An observer traveling at speed v upon a highly relativistic electron sees an incoming low-energy photon at a blue-shifted wavelength

$$\lambda_B = \lambda\sqrt{\frac{c-v}{c+v}}. \tag{3.5}$$

After the interaction, in the rest frame of the electron, the photon has a scattered wavelength

$$\lambda' = 2\lambda_{Compton}\sin^2\frac{\theta}{2} + \lambda_B. \tag{3.6}$$

In the extreme case of photon back-scattering, $\theta = \pi$. Shifting to the rest frame of a terrestrial observatory, these back-scattered photons will have wavelength

$$\lambda_S \sim \lambda'\sqrt{\frac{c-v}{c+v}} \sim \lambda\frac{c-v}{c+v} + 2\lambda_{Compton}\sqrt{\frac{c-v}{c+v}}. \tag{3.7}$$

The wavelength of the initially low-energy photon is shortened, meaning its energy is increased by factor

$$\frac{c+v}{c-v} \sim \frac{(1+v/c)^2}{(1-v^2/c^2)} \sim \frac{E_{e^-}^2}{m_{e^-}^2 c^4}. \tag{3.8}$$

A low energy photon experiences many such up-scatterings to become a VHE gamma-ray.

3.4 BL Lacertae

BL Lacertae (R.A. 22 02 33.3, Dec. +42 16 39) was originally observed in 1926 [23] as an optically bright, variable star in the Lacerta cluster, and was affixed with a moniker following the stellar naming convention. In 1965, this position was detected as a radio source (VRO 42.22.01) at the Vermilion River Observatory [24]. This same group later noted that the source showed an atypically flat radio spectrum. Also in 1965, BL Lacertae and VRO 42.22.01 were resolved to occupy the same sky position. Spectroscopic observations of BL Lacertae [25] showed a continuous spectrum with no emission lines, which at the time was unique for such a luminous quasar object. In 1974, based on characteristic spectral absorption lines, a redshift of $z = 0.07$ was established for BL Lacertae [26]. A lack of emission lines led many to believe that BL Lacertae is a prototype of a new class of quasi-stellar objects [27], but eventually weak emission lines were observed [28]. BL Lacertae thus behaves like a normal quasar albeit at the extreme limit of weak emission line intensity. X-Ray emission from this source was detected in 1979 by the Einstein satellite [29]. During the 1990's, EGRET made an unambiguous detection of 5 GeV gamma-rays from BL Lacertae [5]. The power-law relating flux to photon energy $\frac{dN}{dE} \propto E^{-(2.2 \pm 0.3)}$ (Figure 3.5) was then assumed to extend to higher energies.

If this power-law photon spectrum continues unbroken to higher energies, ground based detectors will also make unambiguous detections of BL Lacertae above their respective energy thresholds. These experiments do not detect BL Lacertae within the TeV gamma-ray regime [11], [8]; evidence that the power-law either steepens significantly in the 10−300 GeV window or that there is a sharp cut off in emission at some critical energy. TeV experiments have postulated that the lack of TeV sources can be attributed to the process $\gamma_{TeV} + \gamma_{CIB} \rightarrow e^+ + e^-$, for which the second photon belongs to the Cosmic Infrared Background. The expected degree of attenuation of BL Lacertae in the VHE regime is approximated in Figure 3.6 [8]. The CIB is modeled using LCDM cosmology (cosmological constant + cold dark matter) which gives a

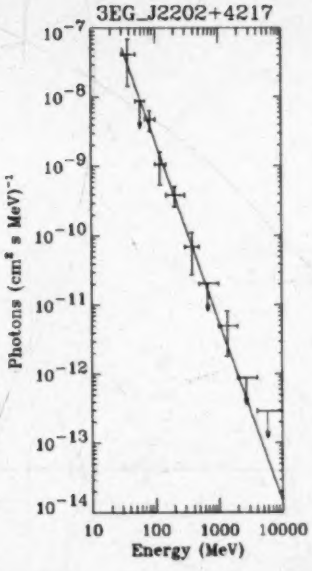

Figure 3.5: Differential flux of BL Lacertae as a function of energy within the EGRET regime.

higher density of CIB photons and as such is more conservative.

The proximity of BL Lacertae effectively nullifies CIB as an attenuating medium for energies within the unopened window ($\sim$ 100 GeV). Whether or not STACEE is able to claim a detection of BL Lacertae above its threshold of 190 GeV, the observation will help to better establish properties intrinsic to BL Lacertae.

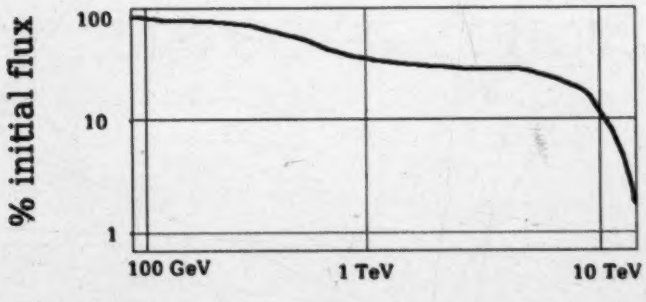

Figure 3.6: CIB attenuation of the observable percentage of flux from BL Lacertae.

3.4.1 Models for BL Lacertae

A spectral energy distribution (SED) relates intensity to wavelength of radiation. To explain the SED of BL Lacertae objects (e.g. Figures 3.7, 3.8), a combination of both synchrotron radiation and radiation energized through the inverse Compton effect can be invoked. Additional consideration must be made to determine the type of particles involved in these processes.

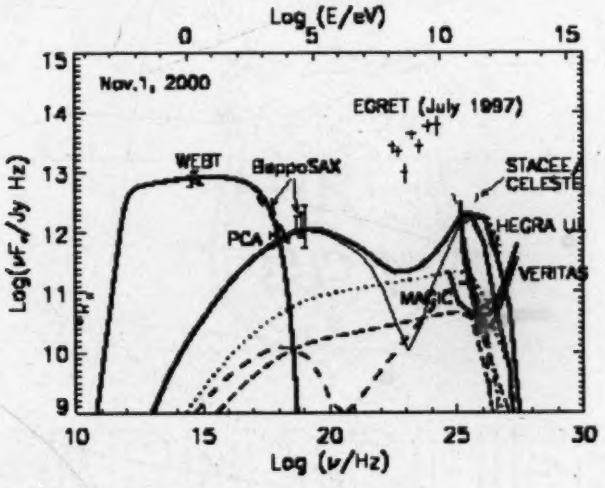

Figure 3.7: Various hadronic model fits to the SED for BL Lacertae multi-wavelength observing campaign during 2000. EGRET data were not part of the campaign and are not considered by the fit.

The low energy peak is characteristic of purely synchrotron radiation. The disagreement between competing models lies in choosing the population of photons that undergo inverse Compton scattering. The Synchrotron Self-Compton (SSC) model postulates that a portion of low energy synchrotron photons undergo Compton up-scattering in energy. The high and low peaks of the SED are in this case both related to the number and energy density of a single group of electrons. Observation has indeed indicated that the two intensities are related, which is strong evidence for SSC.

An alternative is the External Compton (EC) model, which retains low energy synchrotron emission but postulates that the source for low energy photons is a separate population in the torus, rather than a subset of the

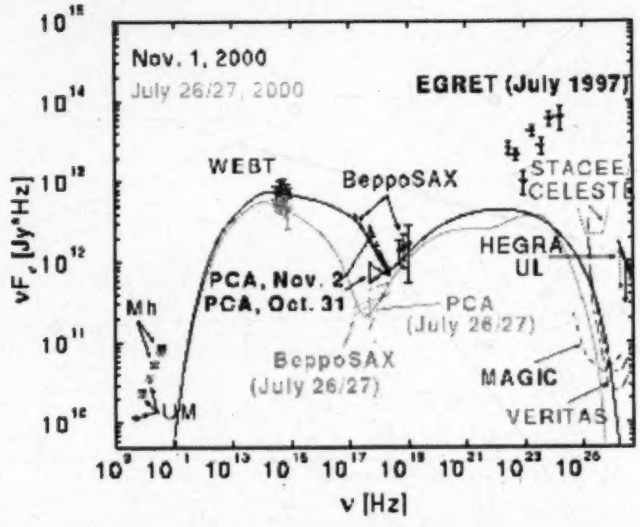

Figure 3.8: Various leptonic model fits to the SED for BL Lacertae multi-wavelength observing campaign during 2000. EGRET data are not part of campaign and are not considered by fit.

synchrotron photons. In fact an admixture of the two models (SSC+EC) is also considered [30].

There is debate about the type of particles that undergo the above processes. Models use either electrons or protons or some combination, a choice which strongly influences the fit of theory to data. Theoretical models of the composition of BL Lacertae have recently been fitted to observational data obtained during a multi-wavelength campaign in 2000 [31]. The campaign included observation of the position of BL Lacertae at radio, optical, x-ray and VHE gamma-ray energies. The researchers were able to place some constraints on both the composition of the relativistic particle population and the emission mechanism. None of the hadronic or leptonic models indicate that STACEE is sufficiently sensitive to detect BL Lacertae. However, hadronic models (Figure 3.7) predict a level of GeV-TeV emission that should be detectable by the second-generation IACTs. Leptonic models (Figure 3.8) predict only weak emission even at the lowest anticipated MAGIC sensitivity of 10 GeV. From these conclusions, a STACEE detection of BL Lacertae is strong support for

hadronic processes driving gamma-ray emission [31].

3.5 Open Questions of AGN

As detailed in the general model, AGN are very strange objects. The model is constructed to explain observations, but there are several underlying principles that warrant further investigation. For example, the highly linear redshift-magnitude relation used to construct Hubble's Law (1929) for galaxies is not obvious for a similar plot showing only AGN [20]. If Hubble's Law is not valid for AGN (or at least not the whole truth), the redshifts may not be attributable entirely to cosmological influences (i.e. the expanding universe). There could be a component of the redshift that results from processes intrinsic to the source itself. If this is true, then AGN are not required to be at such extreme distances. If AGN are closer than Hubble's Law dictates, then their absolute luminosity is reduced. A lower luminosity requirement allows AGN to not be so efficient at producing energy, nor be compact objects. It should however be noted that the linear redshift-magnitude relation requires both Hubble's Law to be valid, and for the objects in the sample to have the same luminosity. It is quite possible that a wide range of luminosities exist for various AGN, thus obscuring the linear relation without invalidating Hubble's Law. Questions like this one are part of the motivation for making as many observations as possible. The wealth of new knowledge provided by the next generation of detectors will complete the gamma-ray SED for many sources, and will serve the development of AGN theory.

Chapter 4

The STACEE Detector

The STACEE detector is an addition to the existing structure of the National Solar Thermal Test Facility (NSTTF) near Albuquerque, USA (34.962° N, 106.509° W). The NSTTF was designed to collect sunlight to conduct solar energy research. The structure (Figure 4.1) is comprised of a tall central tower and an array of 220 reflective mirrors called heliostats. These heliostats are steerable, and can work together to simulate a parabolic mirror that will focus radiation to a collector in the tower. Researchers of solar energy can use this radiation to create steam to drive a turbine. The STACEE instrument has passed through several prototype stages [32], [33], and is now considered to be a complete detector [34]. STACEE makes use of the tower and a subset of 64 heliostats. STACEE is used to collect near-ultraviolet Cherenkov photons. These photons are reflected from the heliostats toward a photomultiplier tube (PMT) array in the tower. The PMT camera and downstream electronics record the energy and position of each photon. Certain conditions must be satisfied to conclude that some distribution of Cherenkov photons result from one incident gamma-ray. Since a ground-based detector cannot be reliably calibrated with an atmospheric gamma-ray source, STACEE relies on detailed simulations to extract scientific results from observations.

4.1 Optics

The goal of STACEE is to observe gamma-rays at a lower energy threshold than other ground-based detectors. The energy threshold of an atmospheric

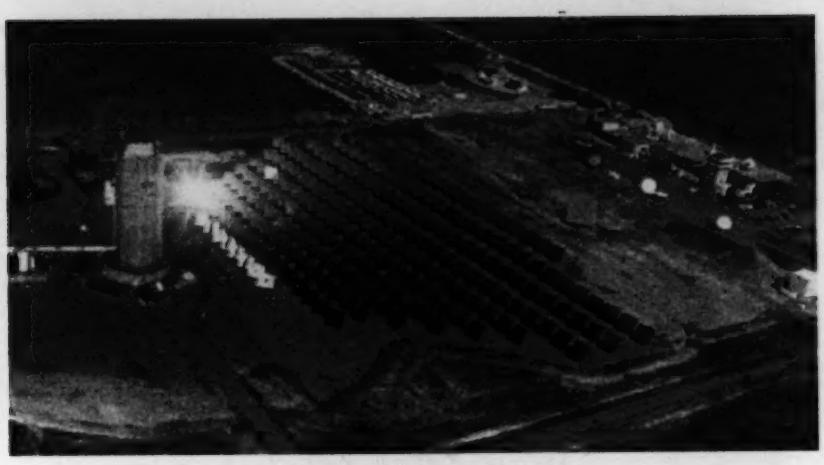

Figure 4.1: The National Solar Thermal Test Facility.

Cherenkov telescope can be shown to behave like

$$E_{th} \propto \sqrt{\frac{\Phi\Omega\tau}{\epsilon A}}. \tag{4.1}$$

Here, Φ is the flux of night sky background light, Ω is the field of view of the instrument, τ is the electronic coincidence window, ϵ is the efficiency of the instrument for collecting Cherenkov photons, and A is the total mirror collection area of the instrument [35]. The easiest way to decrease E_{th} is to increase A. STACEE has a large enough collection area to detect the Cherenkov light from 100 GeV gamma-ray induced electromagnetic cascades. The photon-collecting efficiency of Cherenkov detectors is referred to by the term effective area. The effective area of STACEE is dependent not only on the physical size of the heliostat array, but also on the elevation of the observed source, the energy of the incident gamma-ray, and various hardware efficiencies. Effective area varies in a complicated manner with gamma-ray energy and must be ascertained uniquely for each set of data.

4.1.1 Heliostats

The 64 heliostat array used by STACEE is spread over the 220 NSTTF heliostats in a pattern illustrated by Figure 4.2 [22]. Each heliostat has 37 m^2 of collection area. A heliostat is comprised of 25 facets, each bent into a slightly

parabolic shape by adjustable screws. The facets are made of thick glass, back-surfaced with Aluminum. Each heliostat can be pointed to a range of elevation and azimuthal angles, allowing the entire detector to focus at a single point in the sky. Typically, the detector is focused on a point approximating the first interaction point of the extensive air shower. The shower maxima of air showers at STACEE energies occur around 12.5 km above sea-level.

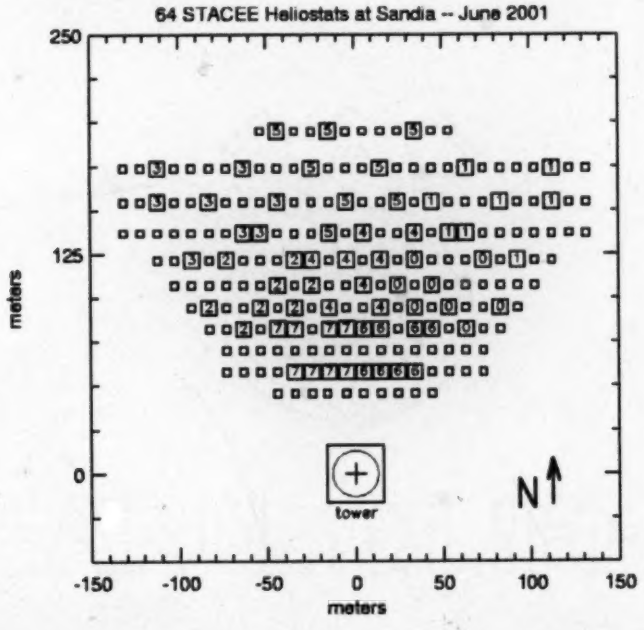

Figure 4.2: The view from directly above the NSTTF. Heliostats used by STACEE are marked by the L1 trigger cluster to which they belong.

4.1.2 Secondary Mirrors and PMT Cameras

Housed in the tower are five secondary mirrors (Figure 4.3). Three of these are positioned 48 m above ground to observe the East, West, and North-central heliostat groupings. Each of these three secondary mirrors is composed of seven hexagonal facets, which are oriented such that they approximate a spherical mirror structure of 1.9 m diameter with a focal length of 2 m. Placed at this focal length are an array of 16 modified photomultiplier tubes (PMTs) called a camera. Each PMT in the camera collects Cherenkov photons reflected from

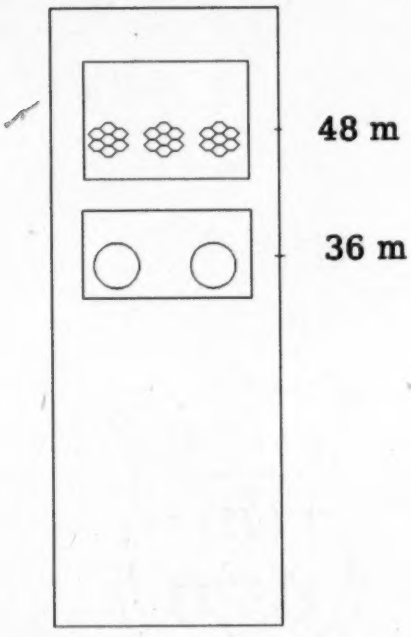

Figure 4.3: The central receiver tower, showing positions of secondary secondary mirrors as height above ground-level.

a single heliostat. Two secondary mirrors are positioned 36 m above ground to observe the South-central heliostats. Each of these is a spherical mirror 1.1 m in diameter with a focal length of 1.1 m. Placed at this focal length are 8 PMTs. A one-to-one mapping between each heliostat and a PMT is crucial to reconstructing the Cherenkov shower-front photon distribution. Measures are implemented to reduce the field of view of each PMT to ensure minimal crosstalk between channels. Each PMT is fitted with an optical concentrator called a DTIRC (Dielectric Total Internal Reflection Concentrator), as in Figure 4.5.

These DTIRCs are made of UV-transmitting acrylic and are precisely molded so that all light entering the convex top will be emitted through the circular base, provided the incident angle is less than some critical value (Figure 4.6 [22]). The DTIRCs are also required to ensure collection of all

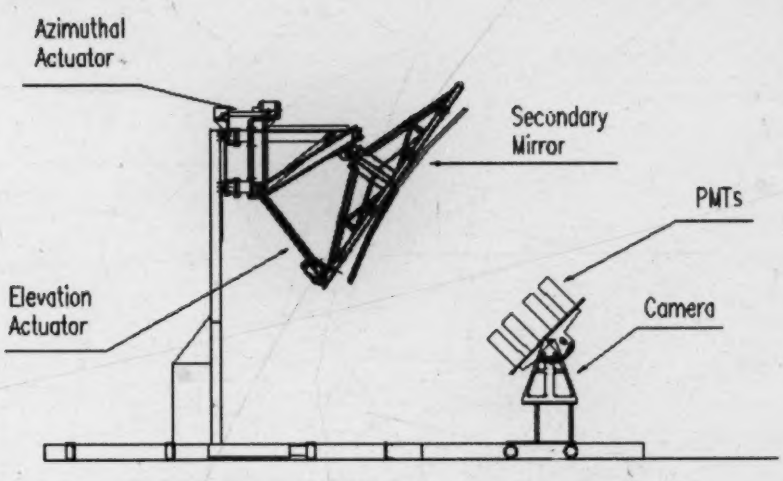

Figure 4.4: A side-on view of secondary mirror and camera.

Cherenkov light, which can be larger in angular size than a standard PMT aperture. The DTIRC collects this light and focuses it into the PMT. Each PMT is assigned a channel number, and the output of all channels are fed into data acquisition software.

4.2 Electronics

Vital to STACEE science is precise information about the energy and the time-of-arrival of each Cherenkov photon. Extracting this information requires both very high speed electronics and a precise knowledge of detector geometry. For a distribution of Cherenkov light to be recorded as an event, a certain fraction of the 64 channels must register a photon hit within a narrow window of time. The use of a narrow timing window is motivated by the structure of a gamma-ray initiated electromagnetic cascade. Since the Cherenkov-radiating electrons and positrons are identical in mass the Cherenkov shower-front will be thin and laterally symmetric. For a hadronic shower, particles of different mass will participate in the construction of a Cherenkov shower-front, leaving the photon distribution thicker and less symmetric than its light-leptonic

Figure 4.5: A cross-section of PMT can assembly.

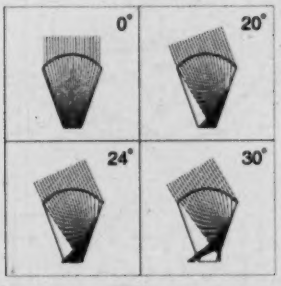

Figure 4.6: A side-on depiction of the angular acceptance of a DTIRC.

counterpart. STACEE employs a two-level trigger system. The 64 channels are grouped by heliostat location into 8 clusters. Within each cluster, a trigger condition is imposed such that 5 of 8 channels must register a hit within a given time interval. This is called a level one (also called L1, or cluster) trigger. Similarly, there must be 5 of 8 simultaneous level one triggers to make a level two (also called L2, or global) trigger. A simple block diagram of STACEE electronics is shown by Figure 4.7. A high voltage supply is connected to the PMTs. The PMT output is amplified then fanned out to the Flash Analog-to-Digital Converters and discriminators. Discriminators are used to eliminate the night-sky background (NSB), passing only Cherenkov events to the trigger. The two-level Trigger/Delay Unit finds all level two events, which are then counted by the VME Scaler. A GPS clock is used to provide a time-stamp for

each event. The VME Scaler and FADC information are merged within the Data Acquisition system.

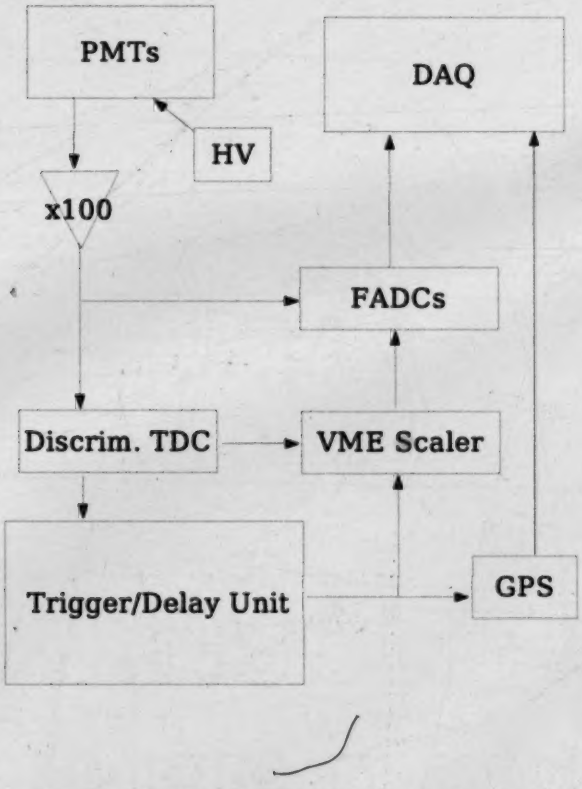

Figure 4.7: Basic STACEE electronics.

4.2.1 Flash Analog-to-Digital Converters

Flash Analog-to-Digital Converters (FADCs) are used to calculate the charge of a PMT pulse for each STACEE channel. FADCs are preferred to standard ADCs because of their speed of operation. Unlike an ADC, which must complete a series of comparator operations, the FADC fans out the incoming pulse and completes all comparator operations in parallel. STACEE, observing in narrow windows of time, must eliminate as much detector deadtime as possible, so that the rate of data acquisition is maximized. STACEE's

high speed (1 GHz) 8-bit FADCs provide measurements necessary for reconstructing the arrival direction and energy of an initial gamma-ray. The use of FADCs has allowed the complete STACEE instrument to achieve more accurate angular resolution and more precise gamma/hadron separation than its prototype versions.

4.3 Simulations

Simulations of STACEE's performance must accurately match real observing conditions for confident results to be stated. The end products of the simulation chain are a detector efficiency and an energy threshold for a given data set. These two quantities combined with the observed rate of gamma-rays lead to a calculation of the total photon flux from the source. Three simulations model what happens during real observation. First, for a gamma-ray photon at some energy it is necessary to predict the number and distribution of Cherenkov photons produced in the extensive air shower. This complicated process is modeled by CORSIKA, a detailed simulation of both the Earth's atmosphere and the high-energy interactions that occur as particles pass through it. Second, knowing a Cherenkov distribution in both energy and position, how many of those photons actually contact a STACEE heliostat? How many of those propagate through to the matching PMT? These questions are answered by sandfield, a detailed STACEE-specific ray-trace program that passes simulated Cherenkov photons from the shower through to a PMT. Since many photons produced in a CORSIKA shower do not contact a heliostat, only a small fraction emerge from sandfield. Third, these are passed to a STACEE-specific electronics simulation which, knowing every photon's energy and arrival time, can tell how many triggered events to expect from a known shower energy. This complete simulation can then be traced in reverse using observational data. Observations are made only in terms of triggered events. Given these, it is possible to reconstruct a potential incident gamma-ray in both energy and position. Knowing the flux of a celestial source over a range of energies then adds to the overall knowledge of AGN and is input

for theoretical models. Since the simulation chain is a large part of STACEE data analysis it is useful to examine each link in more detail.

4.3.1 CORSIKA

STACEE uses the Monte-Carlo air-shower simulation CORSIKA (COsmic Ray SImulations for KAscade) to simulate the evolution of extensive atmospheric air showers [36]. The program was initially developed by the German KASCADE collaboration to do cosmic-ray research [37]. Specifically, CORSIKA simulates atmospheric interactions and decays of nuclei, hadrons, muons, electrons, and photons, up to 10^{20} eV. It gives particle type, energy, location, direction, and arrival time of all secondary particles that are created in the air shower. Especially important to STACEE, CORSIKA accounts for the attenuation of Cherenkov light due to Rayleigh and Mie scattering.

4.3.2 sandfield

sandfield analyzes the distribution of Cherenkov light in every CORSIKA shower. First sandfield chooses, within the dimensions of the heliostat field, a random core location for the shower. By detector geometry and measured efficiencies, sandfield calculates the number of photons that reach each PMT. Owing to a sparse collecting area, very few of the shower photons hit a heliostat. Of these, some will not hit the secondary mirror. Of the remainder, some will miss the PMT entirely or be cut off by the DTIRC's limited field of view. To increase statistics while minimizing computing time, sandfield reuses each CORSIKA shower a user-defined number of times, usually 5−10. When sandfield is finished, a listing of photons and their individual arrival times is passed on to the STACEE electronics simulation elec.

4.3.3 elec

The responsibility for deciding which sets of Cherenkov photons constitute a triggered event ultimately falls to elec. elec begins by simulating PMT output. STACEE uses PMTs with a high quantum efficiency in near-ultraviolet

wavelengths. The ratio of output quanta (photoelectrons) to input quanta (photons) is 0.28. The output from a PMT photoelectrons with combined charge Ge, where G is the measured gain of the PMT, and e is the quantum of electric charge. On its first pass through the data, elec excludes any events which do not contain enough photons to constitute a trigger. Then, elec checks if the charge on each channel is sufficient to pass the discriminator setting. Last, if the level two triggering condition is satisfied a simulated waveform is constructed for each channel. The output from elec resembles raw observational data with the bonus that for simulated data, the initial conditions are known.

4.4 Applying Simulated Results to Real Data

The suite of simulations serves in place of a direct calibration. The main end of the simulations is to determine the efficiency of STACEE to detect gamma-ray-initiated air showers. This efficiency is a mix of both electronic performance and detector geometry, combined to give effective area. The effective area varies greatly with both source elevation and shower energy, and is used to calculate the gamma-ray energy at which STACEE's collecting efficiency is greatest. This energy is called the energy threshold of the experiment. Combining the simulated effective area with the observed gamma-ray rate will yield an upper limit on flux above threshold energy.

4.4.1 Calculation of the Effective Area

Data from all simulated showers that produced triggered events in elec are now resolved into histograms showing trigger probability binned as a function of both energy (E) and hour angle (δ) along the source path. Effective area A_{eff} is defined as

$$A_{eff}(E,\delta) = \pi R_s^2 P(E,\delta), \tag{4.2}$$

where the scattering radius $R_s = 250$ m, and the function P is the probability of an event trigger. At high energies, $P \to 1$ and $A_{eff} \approx \pi R_s^2$. The parameter δ indicates the hour angle along a path specified by a source dec-

lination ($-60 < \delta < 60$), such that $\delta = 0$ is the maximum celestial elevation at source transit. This position also marks the shortest path length traveled, and thus minimal atmospheric attenuation, for gamma-ray showers to the detector. Hour angle is measured as shown in Figure 4.8. The horizon of the observer is shaded. The plane of the page contains the observer's meridian, which is the Great Circle containing the North, South, and Zenith points of view. The North Celestial Pole (P) is the point about which the night sky appears to turn. As a star crosses the observer's meridian, the hour angle is zero, and this is called transit. The hour angle measurement is negative before that point (East of transit) and positive afterward (West of transit).

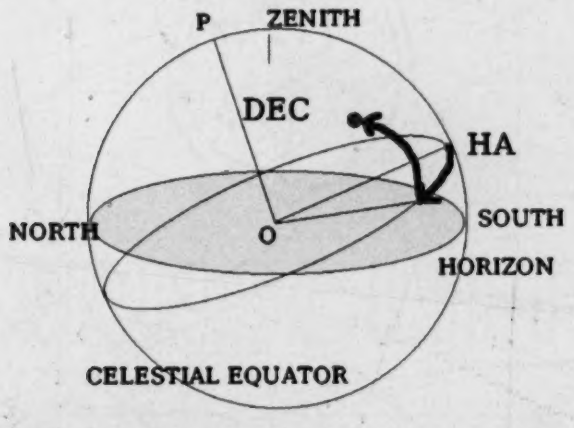

Figure 4.8: An example of hour angle measurement.

4.4.2 Calculation of the Energy Threshold

STACEE defines its energy threshold as the energy at which the differential trigger rate reaches its maximum. This convention has been adopted in lieu of a sharp cutoff in the effective area plot (see Figure 7.5). There is no distinct energy at which the detector is physically insensitive, although showers below 50 GeV will not produce enough Cherenkov light to satisfy STACEE's trigger condition. Differential trigger rate is obtained by multiplying the effective area at an energy by the projected gamma-ray spectral intensity at that energy,

$E^{-\alpha}$, where α is the spectral index for a potential source. The maximum value of the resulting curve (see Figure 7.6) is STACEE's energy threshold for the data set.

Chapter 5

Data Analysis

At high (GeV-TeV) energies, the cosmic ray flux hitting the Earth is isotropic. Cosmic rays can initiate cascades of high energy particles producing Cherenkov radiation (Figure 2.4). This represents a large background to an already intrinsically weak gamma-ray signal. The primary method to remove this background is to exploit the isotropy of the cosmic ray flux by making both an observation pointing at the potential gamma-ray source (ON-source), and an observation pointing along the source path, with the source just out of STACEE's field of view (OFF-source). This is referred to as the ON/OFF method. Subtracting events recorded in the OFF run from those recorded in the ON run should leave a gamma-ray excess, if the source is a gamma-ray emitter at STACEE energies. For an ON run, as the Earth rotates the heliostats adjust to maintain their collective focus on the first interaction point of an air shower initiated by a gamma-ray originating at the source. The ON run lasts for 28 minutes. The heliostats are then allowed two minutes to reset to their initial position, and made to track the same path once more as an OFF run, with the source out of view by 28 minutes in hour angle. During a run, Cherenkov photons are collected as raw data. Information about each photon is written to disk to be used in offline analysis. A calibration program surveys the raw data, converting it to a more accessible form. It is then necessary to look at the distribution of any triggered events. Are trigger rates strongly correlated in time? Are there inconsistencies in the calibration? Did the hardware function properly or were warning flags raised? These questions

are answered by several algorithms, each designed to examine calibrated data from a certain perspective. After necessary cuts are made to the raw data, a remaining excess or deficit in events between ON and OFF runs will result. This, combined with the durations of the two runs, is used to quote a significance for the signal. This ends the observational analysis, and simulations must be used to make further predictions. Each of the stages of data analysis is examined in more detail below.

5.1 stoff

stoff [38] is the STACEE offline data format and the program upon which all data analysis is based. Any raw data read in by the data acquisition system is written in a stoff format and assigned to a relevant grouping of data called a bank. These banks contain specific subsets of raw data, ranging from the heliostat monitoring system to the PMT pulse characteristics. For example, all information from the FADC waveform digitizers is contained in a single bank called DIGI. Bank structure allows easy access to related data quantities.

5.2 Raw Data Calibration

The role of the data calibration program pass0 is to convert raw data quantities into a more useful human-readable form, and to output a calibrated product that can be accessed by the downstream analysis framework. For example, FADC data exists as 1 ns waveform measurements on each of the 64 STACEE channels. These waveforms are a digital representation of PMT analog pulses with time-delimited values ranging from 0−255 digital counts, which are converted to voltage (256 counts = 1 V). Pulse voltages must cross a threshold discriminator value to be considered for the trigger. The discriminator is set to exclude up to 3 σ fluctuations in the NSB. Timing information is necessary to correlate channels to impose the trigger conditions. The photon time-of-arrival, as measured by the FADCs, is calculated by linearly fitting the 1 GHz-sampled waveform to find the precise instant that a pulse crosses threshold as a new Cherenkov event. For every event, a channel baseline volt-

age is calculated by averaging the FADC output for the 400 ns preceding a Cherenkov event. For every Cherenkov event, the pulse width is defined as the number of consecutive samples (at 1 GHz) for which the interpolated waveform is above threshold. pass0 stores all these data to the relevant stoff bank to be used in data analysis. The production of a realistic data product also involves corrections for asymmetry of NSB brightness between ON and OFF halves of a pair. Currently, pass0 is responsible for this field brightness equalization through a process called library padding.

5.3 Field-Brightness Asymmetry

By virtue of its construction, a PMT outputs a signal which is an analog sum of pulses produced by both Cherenkov and night-sky background (NSB) photons. The superimposition of NSB can either increase or decrease the amplitude of the Cherenkov signal. The resultant pulse must then face a discriminator threshold. Cherenkov pulses intrinsically below the threshold might surpass it if there are above-average NSB fluctuations. By the same logic, Cherenkov pulses that should intrinsically cross the threshold may be removed by the discriminator if there are below-average NSB fluctuations. To first order, these two effects occur randomly throughout the data set and will cancel each other were it not for the steep power-law flux-energy dependence of the gamma-ray spectrum. In any sample, there are more low energy gamma-rays available for promotion than high energy gamma-rays available for demotion, resulting in a net increase in signal. This second order process is called the promotion effect [39].

5.3.1 Direct Measurement of the Promotion Effect

Promotion becomes a serious concern if the ON/OFF NSB conditions are very asymmetric. Such asymmetry can be caused, for example, by a star in the field of view, as is the case for the confirmed gamma-ray source Markarian 421 [16]. If not corrected for, the promotion effect might lead to false excesses being observed, or possibly real excesses being suppressed. In either case NSB

conditions need to match to achieve confident results. An intuitive method for matching field brightness is to compare observed excess gamma-ray rate to average PMT anode current difference between the ON and OFF halves of a pair or runs. The result is compared to similar data recorded for several stars, observed as though they were sources of gamma-rays. During operation, STACEE records average values for both anode current I and channel occupancy X for all channels in each run. An average difference ON-OFF of anode current for an entire data set can be estimated by

$$\Delta I_{total} = \frac{\sum_{i=1}^{64} \langle X \Delta I \rangle_i}{\sum_{i=1}^{64} \langle X \rangle_i}, \tag{5.1}$$

where the angular brackets refer to averaging over all runs in a set. The observed excess gamma-ray rate is then plotted against ΔI_{total}. The star rates and currents are plotted to provide a zero signal baseline. If an observation agrees with the star trend, then any gamma-ray excess is entirely attributable to the promotion trend and does not count as signal. Subtracting the mean promotion trend from a signal to obtain the gamma-ray excess is a rough approximation of the true gamma-ray excess. With detailed FADC information, the complete STACEE detector is able to more precisely measure ON/OFF NSB asymmetry.

5.3.2 Library Padding in pass0

The above method is quite general, reflecting the source observing period only on average, as well as the sky conditions for the period of star data collection. FADC data allows for a more detailed analysis of the promotion trend. Analysis and correction is completed during pass0 calibration of data in the following way. A library of pre-recorded FADC traces is recorded using LED signals in the place of real NSB photons. pass0 determines the RMS of background fluctuations during each of the ON and OFF runs. If, for example $RMS_{ON} > RMS_{OFF}$, then the ON run is left alone and a library trace with $RMS_{lib} = \sqrt{RMS_{ON}^2 - RMS_{OFF}^2}$ is added to the OFF run. The background fluctuations now match in both OFF and ON. The trigger condition is then reimposed for each recorded event but at a higher analysis threshold than

before padding. The threshold must be increased because adding traces to events in the low-noise run only increases the likelihood of some event passing offline cuts. The padding process cannot spawn any new events (those in the low-noise run that would have triggered had extra noise been present during the actual run). By raising the analysis threshold, events in the high-noise run which would not have triggered without the noise are effectively removed from the data set.

5.4 Data Quality

An existing program called stoff-pair [40] handles the quality of pass0 data. stoff-pair was developed to standardize STACEE source analysis and continues to be refined and improved as new methods become available. The program examines stoff bank data in both the ON and OFF halves of a matching pair of runs and removes faulty time-sections based on user specifications. The ultimate goal is to remove any time interval of the pair which will yield unreliable estimates of the gamma-ray excess. If a problem occurs in one half of the pair, the misbehaving time interval is removed from both halves. Hardware malfunctions and transient weather can lead to fluctuations in the level-one trigger rate and thus to a false excess or deficit of gamma-ray signal. There is a standard suite of these time cuts applied to ON-OFF pairs.

5.4.1 Data Cuts - Hardware Performance

The hardware cut algorithms are quite intuitive. The program scans through a run, focusing on certain value in a particular bank. When the bank value is read as faulty, a flag is raised until an acceptable value returns. Later analysis ignores flagged sections of a pair. A variety of hardware cuts are considered standard to any analysis of STACEE data, including the flagging of time-intervals during which either FADC data has not been properly stored, or the atmospheric monitoring system has determined that frost has become an impediment to heliostat reflectivity, or a heliostat has not been tracking properly, or the high voltage power supply to the PMTs has malfunctioned,

or padding was not properly implemented. All of these can affect L1 trigger rate and the offending time intervals are removed from further analysis.

5.4.2 Data Cuts - Level One Trigger Rate

Once hardware cuts are completed, the L1 trigger rates of the now improved ON-OFF pair are corrected for any environmental anomalies that may have caused large L1 rate fluctuations in either half of the pair. The principal culprits are varying cloud coverage and interference from stray surface light. The method for removing data with unacceptable L1 rates is statistically implemented. In this analysis the preferred method for cutting on L1 rates is to eliminate time-sections of a pair for which the ON L1 rate or the OFF L1 rate stray from the trend set by the mean of all the time-sections. First, the pair is broken into 30 s intervals, and a plot of OFF-L1 rate versus ON-L1 rate is constructed for each of eight clusters of eight channels. It is necessary to parse the analysis into clusters since the L1 cluster trigger rate varies greatly with the position of the extensive air shower core. An example is shown for one cluster in Figure 5.1.

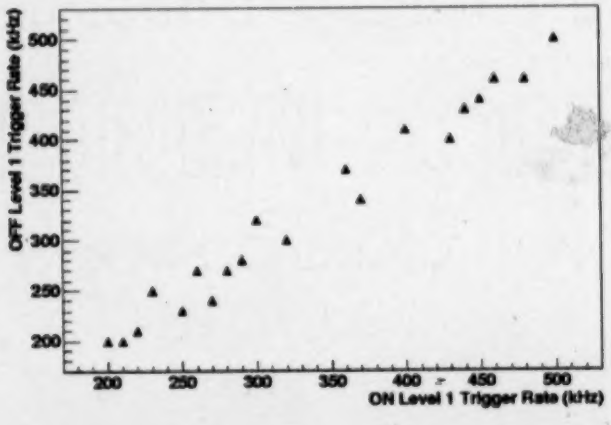

Figure 5.1: Example correlation plot for ON and OFF L1 trigger rates as recorded by one cluster.

Points on this plot should follow a roughly linear trend and not span a large range in rate. The ON and OFF rates are correlated since the positioning of

the heliostat array influences its photon collecting area. Next, each point is assigned an associated angle θ in radians, defined as the angle subtended by the ON-L1 rate axis and a line drawn from the origin to the point in question. Then, a histogram is made for the all cluster values θ and a 2 σ cut is made as shown in Figure 5.2.

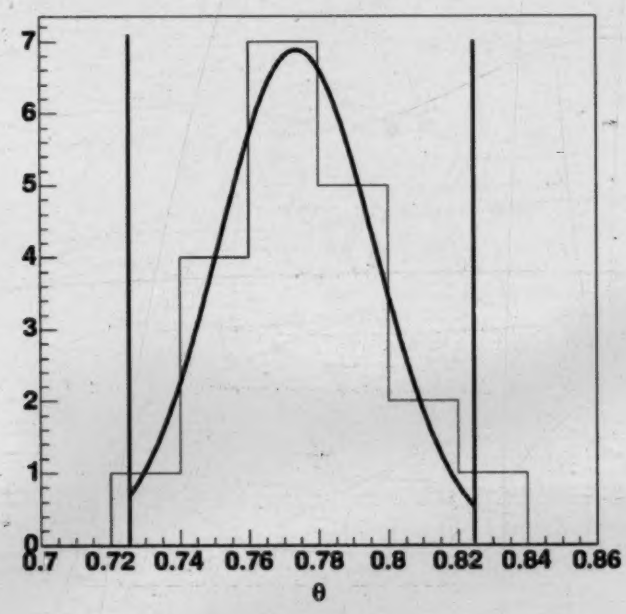

Figure 5.2: Example histogram of θ showing a 2 σ cut on a Gaussian fit.

All outlying points are considered to have unacceptable L1 rates and the offending time intervals are removed from both the ON and OFF runs. The histogram should have a narrow distribution, allowing for more conservative cuts. This marks the end of the data-cutting process; a gamma-ray excess can be extracted from the data, as well as the time-weighted significance of that observation.

5.5 Calculating the Significance

Cleaning the data set using padding and time cuts leaves an excess that can be attributed only to gamma-rays. However, excesses seen by STACEE

are usually only a small fraction of the total triggered events, the bulk of which are NSB background. In this situation it is necessary to consider the possibility that any observed excess can with some probability be attributed to a fluctuation in that background. The quantity that relates excess signal to background fluctuation is called the significance. The significance of an excess is defined as the number of standard deviations (in NSB events) by which the measured signal exceeds the background. Significance (S) is calculated by

$$S = \frac{N_{ON} - (\frac{t_{ON}}{t_{OFF}})N_{OFF}}{\sqrt{N_{ON} + (\frac{t_{ON}}{t_{OFF}})^2 N_{OFF}}}, \tag{5.2}$$

where N_{ON} and N_{OFF} are the number of triggered events after all cuts in the ON and OFF runs respectively, and t_{ON} and t_{OFF} are their corresponding durations [41]. STACEE does not usually claim a detection unless $S \geq 5\sigma$.

Chapter 6

Noise Analysis

To report confident results, especially for the case of weak gamma-ray signals observed at STACEE, it is crucial to quantify all noise in the electronics. This analysis measures noise through examination of FADC output at STACEE. The FADCs are housed in four crates. Each crate contains four boards, with four channels to a board. FADC output is stored as voltage, in units of digital counts, which are sometimes converted to millivolts (256 dc = 1000 mV) depending on the application. Under nominal conditions, FADCs operate at a baseline (pedestal) voltage of around 230 dc. Pedestals vary from channel to channel and must be measured at least once every observing season at STACEE. Each FADC has an adjustable threshold which is used to discriminate Cherenkov events from random NSB fluctuations. An FADC voltage recorded at greater than three standard deviations (3 σ) from the pedestal is treated as a Cherenkov event. When a Cherenkov event occurs, the time and amplitude of the trace are written to disk. Also included with the event are the 192 ns of surrounding FADC trace. Figure 6.1 shows a Cherenkov event crossing the discriminator threshold (solid line).

It is reasonable to want to narrow the discriminator threshold as much as possible. This will increase the energy sensitivity of STACEE by allowing Cherenkov pulses with smaller amplitude to cross the threshold. However, care must be taken not to mistake NSB fluctuations as Cherenkov events. To reduce the discriminator threshold while keeping the 3 σ cut requirement, one must decrease the value of σ. Reducing σ requires a good understanding of

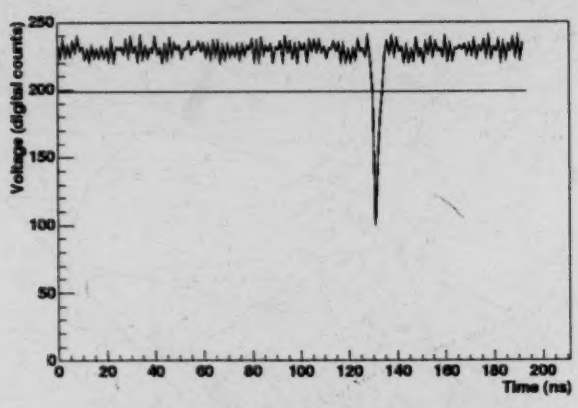

Figure 6.1: FADC trace for a Cherenkov event.

the NSB fluctuations (the total noise) output from the FADCs. The following analysis estimates this noise by examining the pedestal-subtracted FADC output in dc, which is readily accessible through stoff. The data (Run 12645) were recorded continually during a 24 hour period[1]. Run 12645 was taken with the high-voltage supply off, ensuring that no real Cherenkov signal entered the electronics via a PMT. Fake triggers, which contain only NSB pulses, were sent to the FADCs to stimulate data acquisition. The total noise (Σ) is measured by the following rms variation method. At nominal operating conditions, after pedestal-subtraction, average FADC output should be zero. Deviation from zero is attributed to noise. The rms variation method amounts to compiling a histogram of these data and extracting the standard deviation of data. This value is taken to be the total noise in dc. Total noise is understood to be a combination of two noise components. These are the coherent noise (σ_{coh}) which simultaneously affects all channels, and the incoherent noise (σ_{inc}) that is completely random. While random noise is clearly visible in Figure 6.1, coherent noise is a surreptitious systematic effect which has not been previously calculated for the STACEE FADCs. The two noise components add in quadrature such that

[1]November 11, 2003 by J. Zweerink at STACEE.

$$\Sigma^2 = \sigma_{inc}^2 + \sigma_{coh}^2. \tag{6.1}$$

Coherent noise is estimated by a mathematical technique. The incoherent noise is then calculated using Equation 6.1. The results are presented in two parts to answer two separate questions. First, is there a time-dependence of noise on a scale of 24 hours? An affirmative answer indicates the presence of an environmental systematic effect, the cause of which should be found and accounted for, if not eliminated. Second, does noise vary between FADC crates or boards? Some channels are intrinsically noisier than others and this can be dealt with by assigning individual discriminator thresholds to each channel. However, if a crate or board is subject to a large amount of coherent noise, the reason should be ascertained and an appropriate fix implemented. Coherent noise may be reduced by shielding the offending crate or board from stray electromagnetic radiation in the local environment (e.g. from a nearby power source).

6.1 Coherent Noise Estimation Using Alternate Sums

Coherent noise is estimated mathematically, using the method of alternate sums[2]. If x_{ij} is the FADC output in dc for some event i on some channel j, then the average count value μ_j for some channel is simply

$$\mu_j = \frac{1}{N}\sum_{i=1}^{N} x_{ij},$$

where N is the total number of events in the set. Knowing the mean count values for each channel, the deviation D_{ij} of a particular value from that mean

[2]Method developed by Dr. D.M. Gingrich.

can be determined for each of c channels:

$$\begin{aligned} D_{i0} &= x_{i0} - \mu_0 \\ D_{i1} &= x_{i1} - \mu_1 \\ &\vdots \\ D_{i(c-1)} &= x_{i(c-1)} - \mu_{c-1}. \end{aligned}$$

Deviations are calculated for every event i. All values D_{ij} are now be combined into a sum S_i^+, and an alternate sum S_i^- defined below:

$$S_i^+ = \sum_{j=0}^{c-1} D_{ij} \tag{6.2}$$

$$S_i^- = \sum_{j=0}^{c-1} (-1)^j D_{ij}. \tag{6.3}$$

If the total noise is random, then $S_i^+ \approx S_i^-$. If there is a coherent component that causes all channels to shift at once, then $S_i^+ > S_i^-$. The rms variation of these two sums can then be calculated:

$$\sigma_+^2 = \frac{1}{N-1} \sum_{i=0}^{N-1} (S_i^+)^2 \tag{6.4}$$

$$\sigma_-^2 = \frac{1}{N-1} \sum_{i=0}^{N-1} (S_i^-)^2. \tag{6.5}$$

Finally, the coherent noise is:

$$\sigma_{coh} = \frac{\sqrt{\sigma_+^2 - \sigma_-^2}}{c}.$$

6.2 Results - Time Dependence of Noise

During Run 12645, fake triggers were sent through the STACEE electronics at a rate of 0.5 Hz for 24 hours. The total number of recorded events is 40800. The constant input rate makes the event number an equivalent measure of the instantaneous elapsed time of the run. It is then possible to determine the time dependence of noise by parsing Run 12645 by event number. 1700 events are recorded every hour. To get a measure of noise in a particular

hour, those 1700 events are put through the analysis. Total noise is plotted in Figure 6.2 along with its coherent and incoherent components. The coherent noise is not sufficient for total and incoherent noise to be visibly distinguishable on this plot. The mean values and statistical errors from fitting are: total noise (7.25 ± 0.20) dc, incoherent noise (7.24 ± 0.20) dc, coherent noise (0.48 ± 0.01) dc. Figure 6.3 is the same plot magnified about the mean value of coherent noise.

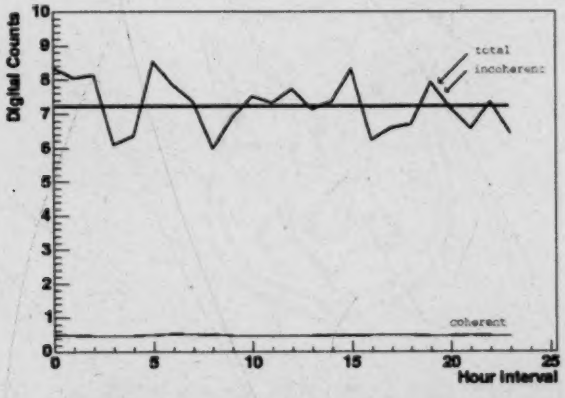

Figure 6.2: Total, incoherent, and coherent components of noise over 24 hours. An average value for both total and incoherent noise is shown.

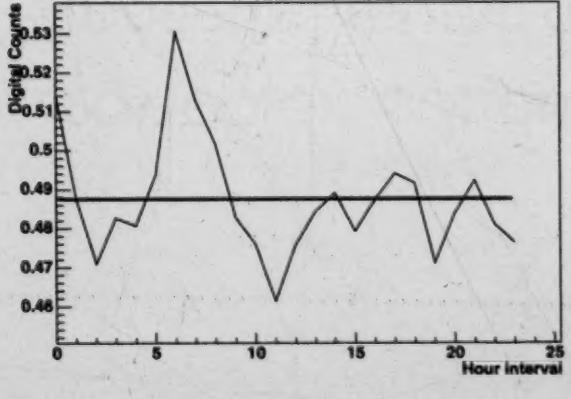

Figure 6.3: Magnified view of Figure 6.2, showing only the coherent noise. An average value for coherent noise is also shown.

6.3 Results - Component Dependence of Noise

To determine the relative noise of each FADC, it is useful to separate the full set of 64 by crate and by board. Crates are assigned a number 0-3 and boards are assigned a number 0-15. A corresponding match to STACEE channel and to hardware channel is given in Table 6.1.

Board	STACEE Channel	FADC Crate	FADC Hardware Channel
0	0-3	0	4-7
1	4-7	0	8-11
2	8-11	0	12-15
3	12-15	0	0-3
4	16-19	1	4-7
5	20-23	1	8-11
6	24-27	1	12-15
7	28-31	1	0-3
8	32-35	2	4-7
9	36-39	2	8-11
10	40-43	2	12-15
11	44-47	2	0-3
12	48-51	3	4-7
13	52-55	3	8-11
14	56-59	3	12-15
15	60-63	3	0-3

Table 6.1: FADC numbering.

The analysis mirrors that of the previous section, but reduces the scope of calculation to only the required channels. The results are shown by crate number (Table 6.2) and by board number (Table 6.3). Additional statistics are provided in Table 6.4.

Crate	Total (Σ)	Coherent (σ_{coh})	Incoherent(σ_{inc})
0	2.86	0.47	2.82
1	2.91	0.51	2.86
2	3.20	0.55	3.16
3	2.25	0.41	2.21

Table 6.2: Noise estimation by crate. Values are given in units of dc.

Board	Total (Σ)	Coherent (σ_{coh})	Incoherent(σ_{inc})
0	0.79	0.32	0.73
1	0.76	0.31	0.69
2	1.14	0.45	1.04
3	2.10	0.79	1.95
4	1.00	0.39	0.92
5	1.57	0.57	1.47
6	1.96	0.66	1.78
7	1.00	0.39	0.92
8	1.13	0.46	1.03
9	2.42	0.77	2.29
10	1.14	0.46	1.04
11	1.23	0.50	1.13
12	1.21	0.48	1.11
13	0.99	0.38	0.91
14	0.88	0.35	0.81
15	1.14	0.45	1.04

Table 6.3: Noise estimation by board. Values are given in units of dc.

6.4 Discussion

The FADC analysis threshold is defined as the minimum pulse height for which a PMT photo-pulse is considered a Cherenkov event, and thus not due to NSB fluctuations. A channel threshold is set at three times the standard deviation of an NSB-only FADC trace on that channel. A standard threshold value is 36 dc (140 mV). The time-averaged coherent noise over all 64 channels in the STACEE experiment is 0.48 dc (Figure 6.3). This is ~1% of the standard analysis threshold. Coherent noise is a persistent effect that essentially shifts the pedestal nearer threshold. Since the analysis threshold is defined in reference to the pedestal, coherent noise effectively raises that threshold. A reduction in coherent noise will thus allow a reduction in analysis threshold. For the FADCs, coherent noise is not a large enough effect to cause disagreement between the time-averaged value of incoherent noise, (7.24 $\pm$ 0.20) dc, from that of the total noise, (7.25 $\pm$ 0.20) dc. Even the complete elimination of coherent noise will not allow substantial reduction of the discriminator thresholds. There is no 24-hour time-dependence of either coherent or total

Boards	Mean = 0.484 dc StDev = 0.147 dc $> \pm 1\sigma$: Boards 0,1,3,6,9 $> \pm 2\sigma$: Board 3
Crates	Mean = 0.485 dc StDev = 0.058 dc $> \pm 1\sigma$: Crates 2,3 $> \pm 2\sigma$: none

Table 6.4: Averaged results, emphasizing components deviating from average component behaviour.

noise. Both data are fit by zero-order trends. The time of night that particular data were recorded is therefore not important in reference to the contribution of coherent noise to the signal. Noise statistics are presented for each board and for each crate. Of particular concern are boards or crates with unusually high coherent noise. Board and crate-averaged estimates of coherent noise are also presented, enumerating boards or crates with coherent noise estimates outside one and two standard deviations (σ) of the mean. Boards 6 and 9 and Crate 2 have coherent noise contributions greater than $+1\sigma$, and Board 3 is greater than $+2\sigma$. High coherent noise in a component is owing either to the component itself, or to the local environment in which the component is housed. More comprehensive tests are required to determine which of these causes is responsible for the behaviour of each component.

Chapter 7

Observations of BL Lacertae

The STACEE detector was used to briefly observe BL Lacertae in the late Fall of 2002. In this chapter are detailed the results of these observations, including analysis of the data set and simulation of the detector effective area, culminating in an upper limit on photon flux above STACEE's energy threshold.

7.1 Data Set

The data set consists of 7 ON/OFF pairs recorded over a thirty day period. The total observation time is 2.54 hours before any quality cuts are made. In Table 7.1 are listed the run numbers, the elapsed time that STACEE followed its targets during the runs, the level-two triggered events recorded, and the significance of the observations.

Run (ON,OFF)	Time ON (s)	Time OFF (s)	Events ON	Events OFF	Sig.(σ)
9462,9463	1426.42	1434.93	9447	9328	1.28
9464,9467	773.52	774.41	3964	3966	0.03
9601,9602	1355.39	1367.55	11025	10758	2.47
9603,9604	1357.02	1383.42	10932	10332	5.52
9605,9606	1392.37	1404.20	9670	9466	2.06
9664,9665	1406.00	1416.40	9309	9130	1.82
9694,9695	1446.68	1456.32	8617	8506	1.28
All	9157.41	9237.21	62964	61486	5.72

Table 7.1: Raw data.

Runs 9462–9467 were recorded during hours where the local sky was de-

scribed by the STACEE operator as hazy. This effect can scatter Cherenkov light such that low energy showers are less likely to trigger the experiment then under clear conditions. Haze effectively raises the energy threshold of STACEE. Poor weather, constant over a period of the entire pair, will lower average level-one trigger rates on both halves of the pair. Poor weather that varies on a time scale less than an hour (e.g. increasing cloud coverage) will cause changes in level-one trigger rate that must be removed by cuts. The pair 9464/9467 contains only half the data of the other pairs due to hardware failures during Run 9465 which caused the experiment to halt taking data and a new run to begin. This explains the non-sequential numbering of this pair.

7.2 Cuts

Time cut algorithms scan through each run looking at a particular stoff quantity, flagging off regions of abnormality. For this data set, three time cut algorithms were used to clean the data. First, all data were cut for time intervals during which one or more heliostats reported a tracking error. A tracking error is reported if the difference between source position and heliostat pointing surpasses a critical value. Removal of these time intervals is important because when not all heliostats are working together, the physical detector is behaving differently than its simulated counterpart. Second, all data were cut for time intervals in which FADC data was not recorded. This is important since library padding relies on such information to be properly implemented. Third, all data were cut for which level-one trigger rate on one or more clusters deviated from the run-averaged value by 2 σ, for reasons discussed in Chapter 4. After cuts a net excess of gamma-ray events remains. This excess is combined with the total duration of observations to quote a significance for the signal. Pair-wise significances, as well as the number of triggers in the ON and OFF halves of each pair, are included in Table 7.2.

At the position of BL Lacertae STACEE observes 1001 gamma-ray events, above a background of 40987 cosmic ray events, during an observing time of 5938.9 s ON-source. The significance of the observations is calculated [41] to

Run (ON,OFF)	Time ON (s)	Time OFF (s)	Events ON	Events OFF	Sig. (σ)
9462,9463	1269.62	1276.93	8421	8320	1.15
9464,9467	206.86	205.70	1023	1081	-1.39
9601,9602	1182.31	1194.43	9699	9414	2.77
9603,9604	721.10	734.90	5843	5500	4.23
9605,9606	679.12	685.09	4837	4696	1.87
9664,9665	1325.09	1334.84	8786	8618	1.76
9694,9695	554.80	557.39	3379	3358	0.45
All	5938.90	5989.27	41988	40987	4.7

Table 7.2: Final data.

be 4.7 σ. Since most of the excess is due to one pair, we do not claim a signal. A time-weighted plot of pair-wise significance is shown in Figure 7.1.

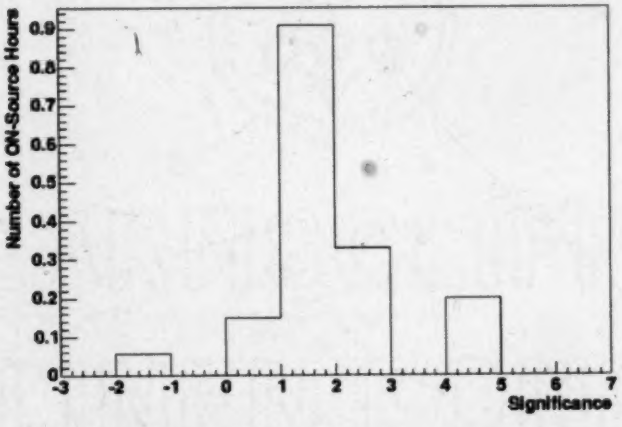

Figure 7.1: Exposure-weighted histogram of pair significances.

Also shown is the light-curve of the data set (Figure 7.2), relating gamma-ray events recorded per minute to the corresponding day of observation. To obtain an upper limit on the flux, all results are combined as a single net excess rate of gamma-ray photons.

7.3 Field Brightness Asymmetry

ON/OFF field brightness asymmetry can be estimated by direct measurement [16] and corrected by using library padding (see Chapter 5 for details).

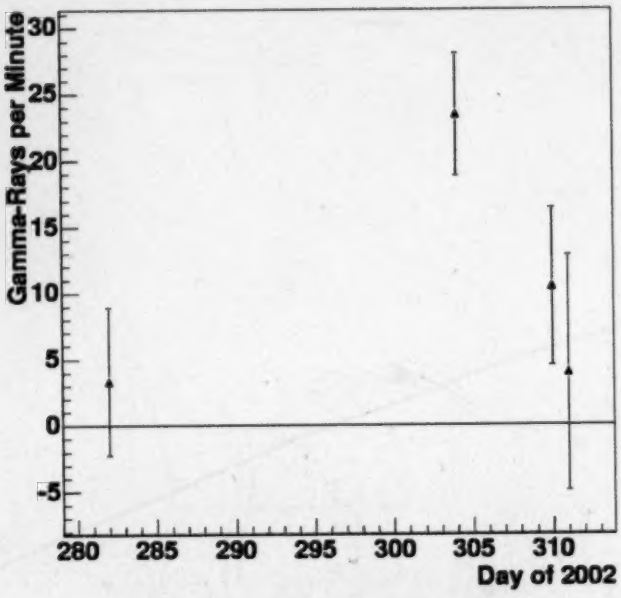

Figure 7.2: BL Lacertae light-curve.

The data were padded during the pass0 calibration. Results in Table 7.1 include this correction. Field brightness asymmetry is not a serious factor in observations of BL Lacertae, a fact most readily demonstrated by the method of direct measurement. Characteristic anode current is 1.05 μA and excess rate is (13.6 $\pm$ 2.9) min^{-1}. Figure 7.3 demonstrates that BL Lacertae does not lie on the promotion trend represented by the linear fit to star data. The dashed lines represent 1 σ statistical errors on the fit, which is constrained to pass through the origin.

Invoking library padding during data calibration does not eliminate the gamma-ray excess. This demonstrates agreement between direct measurement of the promotion effect and the more precise method of library padding. A gamma-ray excess at the position of BL Lacertae can be attributed entirely to that source. Since there is no star in the field of view of BL Lacertae, this result is consistent with expectations. This discussion of field brightness asymmetry is thus included as a check, showing that no correction is necessary.

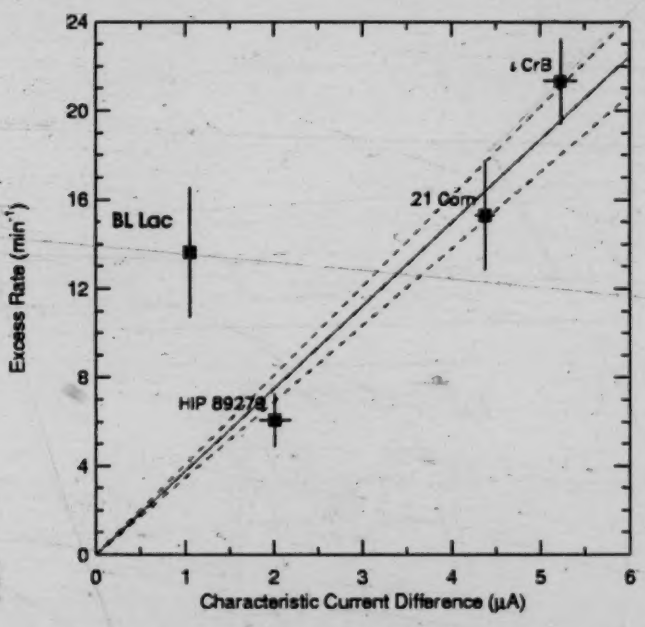

Figure 7.3: Promotion trend: excess trigger rate as a function of (ON-OFF) anode current difference.

7.4 Simulation Inputs

Observational data must be combined with simulations to calculate an upper limit on flux. The STACEE simulation chain is explained in Chapter 3. Here are presented the input parameters that best describe the observational data.

7.4.1 CORSIKA Input

At gamma-ray energies detectable to STACEE, the number of particles in an electromagnetic cascade is small enough that it is not computationally prohibitive to keep track of them all. Hence, CORSIKA was used without invoking the thinning option typically used when studying high energy cosmic ray showers, for which tracking all resultant particles is more costly. Showers are generated using the same sky positions at which real observations are made. At each of 45 positions a suite of showers is generated. By energy, the distribution of showers is listed in Table 7.3 (e.g. fifty 20 GeV showers were

thrown at each of 45 angle settings, along the path of BL Lacertae).

N showers (×45)	Energies (GeV)
50	20,30,40,50,60
40	70,80,90,100
30	110,120,130,140,150,160,170,180
20	200
10	250,300
5	400,500,750,1000
3	1500,2000,5000

Table 7.3: Energy distribution of showers generated.

A total of 32355 gamma-ray showers were generated by CORSIKA. The number of showers generated is greater for low energy gamma-rays because Cherenkov photon flux is proportional to energy and low energy showers have less chance of triggering the detector.

7.4.2 sandfield Input

sandfield was set to re-use each CORSIKA gamma-ray shower ten times. This allows high statistics while using the time-intensive CORSIKA program as little as possible. It has been demonstrated [22] that a tenfold re-use will not introduce unwanted and non-physical systematics which could bias results. sandfield projects on the array a random core location for each of the 10 shower clones. Core location is restricted to within 250 m of the geometric centre of the detector. The sandfield program depends on established STACEE geometry and does not require much user input apart from the CORSIKA files.

7.4.3 elec Input

elec is driven by a parameterized input run card. These parameters define the running conditions of the experiment. It is crucial that the parameters match those measured during the particular observing season. The run card is created with an existing script [40] that examines experimental data and duplicates average running conditions at a range of observation angles. Angular separation is an important consideration since STACEE response varies

non-trivially with the angle to which the detector is pointed. The entire BL Lacertae data set is combined in Figure 7.4, included to demonstrate this point. L2 trigger rate is plotted against integer hour angle of observation. All observations were made West of transit. Error bars on the plot are calculated by dividing the rate by the significance of the observation at that point. As BL Lacertae sets, rate generally decreases for a both low and high-rate periods of observation, a trend which motivates accurate modeling of detector response.

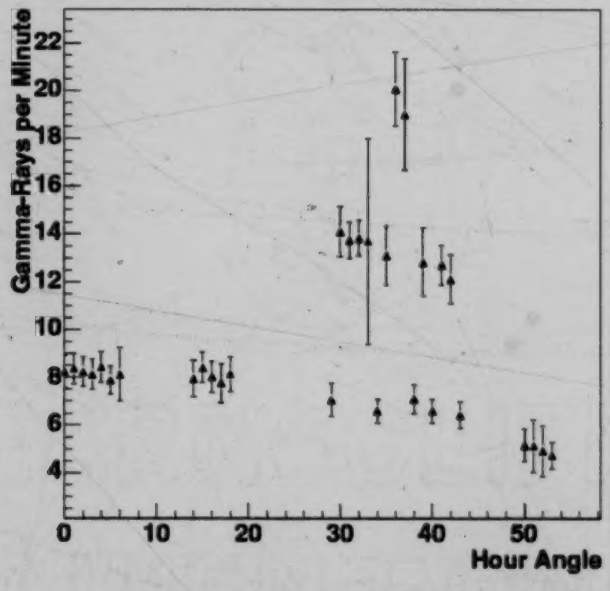

Figure 7.4: L2 trigger rate as a function of hour angle.

7.5 Flux

This section begins by calculating STACEE's effective area at discrete incident gamma-ray photon energies. A few simple calculations then lead to the integral photon flux above energy threshold. STACEE effective area is calculated by Equation 4.2 using efficiencies estimated by elec. The calculation is repeated at several hour angles (HA) along the path of the source. These are then be combined to give the single HA-averaged effective area curve displayed in Figure 7.5.

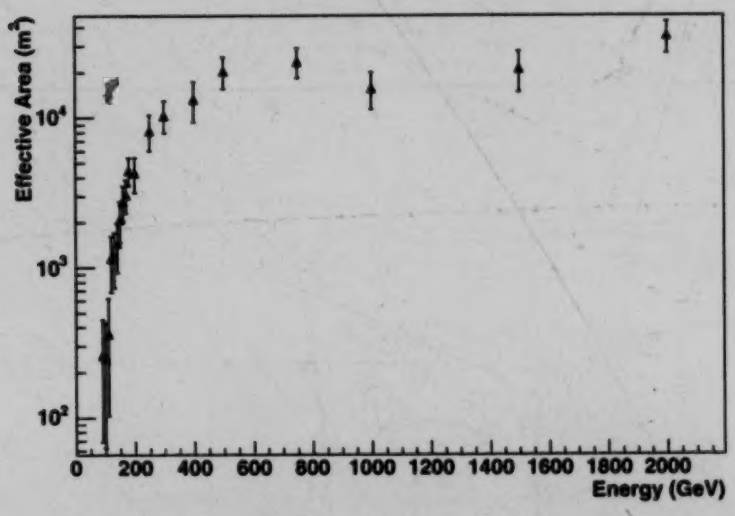

Figure 7.5: HA-Averaged STACEE effective area plot for the positions of the BL Lacertae observations.

The error bars are statistical, and reflect a range of effective areas for each energy, as calculated by the simulation. Above 500 GeV, hardware and detector geometry efficiencies become less inhibiting, and the effective area is simply the angle-projected physical area of the detector. Related to the effective area is the energy threshold at which the STACEE detector becomes sensitive to gamma-rays. The energy threshold depends on both the effective area and the projected spectrum for a specific source. At STACEE this threshold is defined as the maximum of a the differential trigger rate. This rate is a multiplicative combination of the effective area curve and a flux-energy curve with a source-specific spectral index. Although STACEE is sensitive to gamma-rays below this threshold, the suite of showers used in the simulation (Table 7.3) triggered no events below 90 GeV. The differential trigger rate for BL Lacertae is plotted in Figure 7.6, using a spectral index $\alpha = 2.4$. The Whipple collaboration has constrained $\alpha \geq 2.4$ for TeV emission [11], a result that does agree within error to the index proposed by EGRET ($\alpha = 2.2 \pm 0.3$). The error bars propagate from the effective area plot. The STACEE energy threshold is 190 GeV.

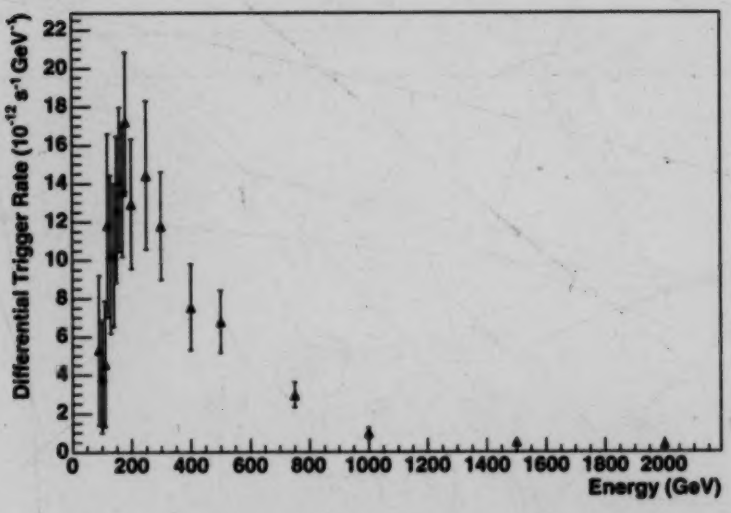

Figure 7.6: Differential trigger rate as a function of energy.

With this information in hand, the flux calculation can begin. The differential flux is defined as

$$\frac{dN}{dE} = C\left(\frac{E}{100\ \text{GeV}}\right)^{-\alpha}, \tag{7.1}$$

where C is a normalization constant and α the spectral index. The rate of gamma-ray events is related to effective area by

$$R_\gamma = \int_0^\infty dE \frac{dN}{dE} A_{eff}(E). \tag{7.2}$$

The calculated gamma rate R_γ is an upper limit on measured rate, accounting for the expected fluctuations in the background. The observed number of events is $N = N_{ON} - \left(\frac{t_{ON}}{t_{OFF}}\right) N_{OFF}$, and the expected background fluctuation is $\sigma = \sqrt{N_{ON} + \left(\frac{t_{ON}}{t_{OFF}}\right)^2 N_{OFF}}$. The limiting number of events comprising the gamma-ray signal N_{lim} can be calculated using the bounded upper limit method [42]

$$\beta = \frac{\int_0^{N_{lim}} e^{-(x-N)^2/2\sigma^2} dx}{\int_0^\infty e^{-(x-N)^2/2\sigma^2} dx}, \tag{7.3}$$

where $\beta = 0.95$ for a 95% confidence level. The limiting rate is $R_\gamma < N_{lim}/t_{ON}$. For BL Lacertae (Table 7.2), the 95% CL rate limit is $R_\gamma < 0.320$ Hz. Integral flux is then calculated by

$$\Phi(E > 190 \text{ GeV}) = \int_{190}^{\infty} dE \frac{dN}{dE}. \tag{7.4}$$

Finally,

$$\Phi(E > 190 \text{ GeV}) < 2.4 \times 10^{-9} \text{ cm}^{-2} \text{ s}^{-1}. \tag{7.5}$$

The dominant uncertainty in the above result is not attached to this flux, but rather to the energy threshold at which the flux is reported.

7.5.1 Energy Threshold Uncertainty

In previous STACEE publications it is shown that the dominant uncertainty in flux measurement is the energy threshold of the experiment [6], [22]. There are several sources of systematic error that will affect the energy scale of the effective area curve, which by definition will shift the energy threshold. These systematics include heliostat reflectivity measurements, air-shower simulations, PMT gain measurements, and PMT quantum efficiency. Accounting for these systematic errors rescales the effective area such that $A_{eff} = A(E') = A(\beta E)$, where β is the ratio of the true photon throughput of the detector to its nominal photon throughput. Nominal photon throughput refers to the collecting efficiency represented by the effective area calculated earlier in this chapter. For a perfectly calibrated detector $\beta \sim 1$. The various uncertainties in STACEE's calibration can be combined and expressed as an error $\Delta\beta$ such that $\beta = 1 \pm \Delta\beta$. As estimated elsewhere [22], $\Delta\beta = 0.20$ for the season during which BL Lacertae was observed. It follows that

$$E_{threshold} = 190(1 \pm \Delta\beta) \approx (190 \pm 40) \text{ GeV}. \tag{7.6}$$

7.6 Discussion

The important results of the observations of BL Lacertae are summarized in Table 7.4. The flux calculated for BL Lacertae can now be compared to results at other wavelengths of the electromagnetic spectrum. Combining data

Total Significance of Observation	$+4.7\ \sigma$
Energy Threshold of STACEE	(190 ± 40) GeV
Integral Flux above Threshold (95% C.L. limit)	$<2.4\times10^{-9}$ cm^{-2} s^{-1}

Table 7.4: Summary of the important results of BL Lacertae observations.

from several detectors sensitive to various wavelengths is the goal of the multi-wavelength campaign. In 2000 a multi-wavelength campaign on BL Lacertae resulted in the simultaneous spectral energy distribution described in Chapter 2. The STACEE observations discussed in this thesis were not made as part of a multi-wavelength campaign. The most recent VHE gamma-ray results for BL Lacerate are summarized in Table 7.5.

Experiment	Threshold	Flux (cm^{-2} s^{-1})
STACEE	190 GeV	$<2.4\times10^{-9}$
CAT [11]	300 GeV	$<1.14\times10^{-11}$
Whipple [11]	350 GeV	$<5.3\times10^{-12}$
HEGRA [8]	580 GeV	$<4.5\times10^{-12}$

Table 7.5: BL Lacertae flux for several VHE gamma-ray experiments.

A gamma-ray spectral energy distribution for BL Lacertae is shown in Figure 7.7. Plotted with the VHE results is the EGRET flux measured at 100 MeV. Also plotted is a curve following $E^{-2.4}$, constrained to the EGRET result. This curve shows that based on the reported sensitivity of VHE experiments, BL Lacertae should be detectable at TeV energies. The VHE experiments all place upper limits below this power-law, and this null result indicates that the power-law either steepens or cuts off at a lower energy. The STACEE upper limit agrees with the predicted spectrum. The significance of the STACEE observation is large enough that while the observations do not represent a detection, an upper limit using these observations will be large and thus less restrictive to spectral modelling than upper limits established with lower significance observations.

A measured gamma-ray rate is based on both the total gamma-ray excess, and the total time of observation. This is a good approximation if there is

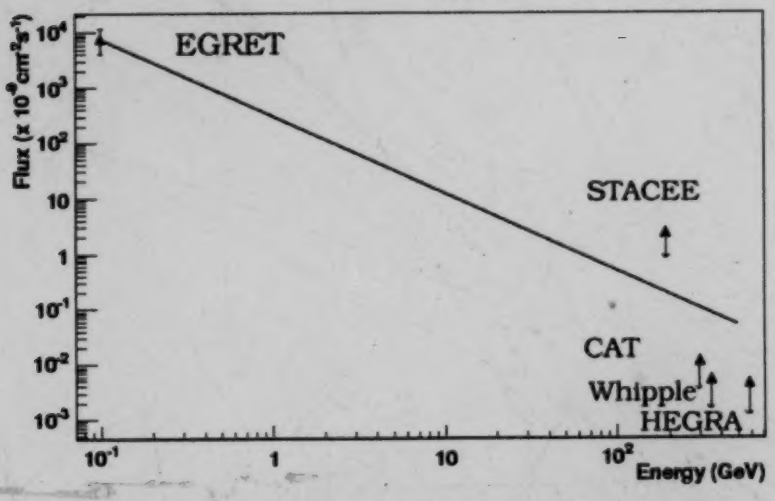

Figure 7.7: Gamma-Ray flux versus energy for BL Lacertae. Except for the EGRET detection, these are upper limits only.

a well-defined light-curve. The BL Lacertae light curve (Figure 7.2) contains very few points, such that each point has a significant effect on a mean value of the curve. One day shows particularly strong gamma-ray emission. It is possible that this is an observation of BL Lacertae during a period of flaring at gamma-ray energies. It should be reinforced that the observing conditions for this day were very good.

Chapter 8

Conclusion

We have presented the results of two investigations. The first is an analysis of observations of BL Lacerate made by STACEE in 2002. The second is a calculation of the noise in the STACEE electronics, focusing specifically on the coherent component of noise.

STACEE observations suggest gamma-ray emission from BL Lacertae. However, the data set is too small and the daily gamma-ray rates are too disparate for this to be considered a detection. We place a 95% confidence level upper limit on photon flux above 190 GeV at 2.4×10^{-9} cm^{-2} s^{-1}. The upper limit agrees with the predicted gamma-ray spectrum. The high significance of the observations (4.7 σ) makes this upper limit a poor constraint to spectral modelling. Based on the current models for BL Lacertae, this result suggests a hadron-initiated gamma-ray emission mechanism at this source.

We have shown that coherent noise is not a significant component of the total noise in the STACEE electronics. Neither the total noise nor the coherent noise show non-random fluctuations about a mean value. There are no long-term trends over a period of 24 hours. The average coherent noise is (0.48 $\pm$ 0.01) digital counts. This is $\sim$1% of the analysis threshold that discriminates Cherenkov photons from NSB fluctuations. Coherent noise shifts the nominal operating voltage towards this threshold. The reduction of coherent noise is desirable if such a reduction allows a lowering of the analysis threshold, essentially a lowering of the overall energy threshold of STACEE. The average values for total and incoherent noise are (7.25 $\pm$ 0.20) digital

counts and (7.24 ± 0.20) digital counts, respectively. We have also shown that coherent noise varies between subsets of the electronics. Further investigation of each component is required to determine whether this variation is intrinsic or the result of electromagnetic radiation in the local enviroment.

STACEE is designed to detect evidence of astrophysical gamma-rays at the lowest energies observable at Earth. The observations of BL Lacertae at 190 GeV are among the lowest energies to date. The evidence for gamma-rays near this energy may foretell the detection of BL Lacertae by the next generation of Cherenkov telescopes. Throughout its development, a primary goal of STACEE has been to lower the energy threshold of the experiment. The results contained in this thesis demonstrate that the reduction of coherent noise is not a profitable method of lowering STACEE's overall energy threshold.

Bibliography

[1] Martin Harwit. *Astrophysical Concepts 3rd ed.* Springer, 1998.

[2] D.J. Thompson *et. al.* "Calibration of the Energetic Gamma-Ray Experiment Telescope for the Compton Gamma-Ray Observatory". *Astrophysical Journal Supplemental*, vol. 86:p. 629, 1993.

[3] W.S. Paciesas *et. al.* "The Fourth BATSE Gamma-Ray Burst Catalog". *astro-ph/9903205*, 1999.

[4] Web page. http://cossc.gsfc.nasa.gov/egret/.

[5] R.C. Hartman *et. al.* "The Third EGRET Catalogue of High-Energy Gamma-Ray Sources". *Astrophysical Journal*, vol. 123:p. 79, 1999.

[6] S.M. Oser. *High Energy Gamma-Ray Observations of the Crab Nebula and Pulsar with STACEE.* Ph.D. thesis, University of Chicago, 2000.

[7] T.C. Weekes *et. al.* "Observation of TeV gamma-rays from the Crab Nebula using the atmospheric Cerenkov technique". *Astrophysical Journal*, vol. 342:p. 379, 1989.

[8] F.A. Aharonian *et. al.* "HEGRA Search for TeV emission from BL Lacertae Objects". *Astronomy and Astrophysics*, vol. 353:p. 847, 2000.

[9] T. Yoshikoshi *et. al.* "Present Status of the 7/10 m Telescope of CANGAROO II". *Astroparticle Physics*, vol. 11:p. 267, 1999.

[10] Rene A. Ong. "The Status of VHE Astronomy". *astro-ph/0304336*, 2003.

[11] M. Catanese *et. al.* "Detection of Gamma-Rays with $E > 100$ MeV from BL Lacertae". *Astrophysical Journal*, vol. 480:p. 562, 1997.

[12] T.C. Weekes *et. al.* "VERITAS: the Very Energetic Radiation Imaging Telescope Array System". *astro-ph/0108478*, 2002.

[13] N. Geherels *et. al.* "GLAST: The Next-Generation High-Energy Gamma-Ray Astronomy Mission". *Astroparticle Physics*, vol. 11:p. 277, 1999.

[14] M. de Naurois *et. al.* "Measurement of the Crab flux above 60 GeV with the CELESTE Cherenkov Telescope". *Astrophysical Journal*, vol. 566:p. 343, 2002.

[15] S.M. Tripathi *et. al.* "The Keck Solar Two Gamma-Ray Telescope and observations of the Crab Nebula". *Bulletin of the American Astrophysical Society*, vol. 34:p. 676, 2002.

[16] L.M. Boone. *Observations of Markarian 421 with STACEE.* Ph.D. thesis, University of California, Santa Cruz, 2002.

[17] Julie E. McEnery *et. al.* "GLAST: Understanding the High Energy Gamma-Ray Sky". *astro-ph/0406250*, 2004.

[18] Denis Bastieri *et. al.* "An AGN Observation Catalogue For the MAGIC Cherenkov Telescope". *in Proc. 28th Int. Cosmic Ray Conf.(Japan)*, page 2555, 2003.

[19] F. Aharonian *et. al.* "Very High Energy Gamma-Rays from the direction of Sagittarius A". *Astronomy and Astrophysics*, vol. 425:p. L13, 2004.

[20] A.K. Kembhavi and J.V. Narlikar. *Quasars and Active Galactic Nuclei.* Cambridge University Press, 1999.

[21] D. Horan *et. al.* "Constraints on the Very High Energy Emission from BL Lacertae Objects". *astro-ph/0311397*, 2003.

[22] R.A. Scalzo. *Observations of EGRET Blazar W Comae with STACEE.* Ph.D. thesis, University of Chicago, 2004.

[23] C. Hoffmeister. "354 neue Veranderliche". *Astronomische Nachricten*, vol. 236:p. 233, 1929.

[24] J.M. Macleod *et al.* "A 610.5 MHz survey of the sky between declinations +40 and +44 degrees". *Astronomical Journal*, vol. 70:p. 756, 1965.

[25] D. DuPuy *et. al.* "Optical Observations of BL Lac = VRO 42.22.01". *Astrophysical Journal*, vol. 156:p. L135, 1969.

[26] J.B. Oke and J.E. Gunn. "The Distance of BL Lacertae". *Astrophysical Journal*, vol. 189:p. L5, 1974.

[27] P.A. Strittmatter *et. al.* "Compact Extragalactic Nonthermal Sources". *Astrophysical Journal*, vol. 175:p. L7, 1972.

[28] R.C. Vermeulen *et. al.* "When is a BL Lac not a BL Lac?". *Astrophysical Journal*, vol. 452:p. L5, 1995.

[29] J.T. Pollock *et. al.* "Long-term optical variations of 20 violently variable extragalactic radio sources". *Astrophysical Journal*, vol. 84:p. 1658, 1979.

[30] M. Bottcher, R. Mukherjee, and A. Reimer. "Predictions of the High-Energy Emission from BL Lacertae Objects". *Astrophysical Journal*, vol. 581:p. 143, 2002.

[31] M. Bottcher and A. Reimer. "Modeling the Multi-wavelength spectrum and variability of BL Lacertae in 2000". *Astrophysical Journal*, vol. 609:p. 576, 2004.

[32] D.S. Hanna *et. al.* "The STACEE-32 Ground Based Gamma-Ray Detector". *Nucl. Inst. Meth A*, vol. 491:p. 126, 1988.

[33] C.E. Covault *et. al.* "The Status of the STACEE Observatory". *in Proc. of the 27th ICRC (Hamburg)*, vol. 1:p. 2810, 2001.

[34] D.M. Gingrich *et. al.* "The STACEE Ground-Based Gamma-Ray Detector". *in Proc. of the IEEE Nuclear Science Symposium 2004 (Rome)*, 2005 (in print).

[35] Trevor C. Weekes. "Very High Energy Gamma-Ray Astronomy". *Physics Reports*, vol. 160:p. 1, 1988.

[36] C. Muller. "CORSIKA for STACEE - Users Manual". *STACEE Internal Collaboration Note 05-02*, 2005.

[37] D. Heck *et. al.* *CORSIKA: A Monte Carlo Code to Simulate Extensive Air Showers.* Forschungszentrum Karlsruhe GmbH, Karlsruhe, Germany, 1998.

[38] J. Boehm, N. Kundtz, and C. Covault. "Release of stacee-banks-2002 data processing package". *STACEE Internal Collaboration Note 02-12*, 2002.

[39] L.B. Boone. "Field Brightness Asymmetries: A First Look". *STACEE Internal Collaboration Note 03-05*, 2003.

[40] D. Bramel. "Analysis Chain with stoff-pair". *STACEE Internal Collaboration Note 04-03*, 2004.

[41] T.P. Li and Y.Q. Ma. "Analysis Methods for Results in Gamma-Ray Astronomy". *Astrophysical Journal*, vol. 272:p. 317, 1983.

[42] Particle Data Group. Review of Particle Physics. *Phys. Rev. D*, vol. 592:p. 283, 2004.